Title	Stochastic Physiological Gaze-evoked Nystagmus in Healthy People During Fixational Eye Movements at Small Gaze Eccentricities: Characterization of Gaze Dynamics and Neuromechanical Modeling
Author(s)	Ozawa, Makoto
Citation	大阪大学, 2022, 博士論文
Version Type	VoR
URL	https://doi.org/10.18910/89651
rights	
Note	

Stochastic Physiological Gaze-evoked Nystagmus in Healthy People During Fixational Eye Movements at Small Gaze Eccentricities: Characterization of Gaze Dynamics and Neuromechanical Modeling

Makoto Ozawa

September 2022

Stochastic Physiological Gaze-evoked Nystagmus in Healthy People During Fixational Eye Movements at Small Gaze Eccentricities: Characterization of Gaze Dynamics and Neuromechanical Modeling

A dissertation submitted to

THE GRADUATE SCHOOL OF ENGINEERING SCIENCE

OSAKA UNIVERSITY

in partial fulfillment of the requirements for the degree of

DOCTOR OF PHILOSOPHY IN ENGINEERING

By

Makoto Ozawa

September 2022

Abstract

Our eyes involuntarily and slightly keep moving even when we try to fix the gaze position. The gaze fluctuation during fixation is called fixational eye movements (FEyeM). It consists of two eye movements: a slow movement like a Brownian motion called drifts-tremor (DRT) and a ballistic movement called microsaccade (MS) with a mean saccadic amplitude of about 0.3° and a mean inter-MS interval of about 0.5 s. Although the importance of FEyeM in visual perception and cognition is becoming to be clear, the mechanism of their motor control is not well understood. Not a few people exhibit oscillatory eye movements when gazing at an eccentric position (far from the front-facing position). This oscillatory eye movement is called gaze-evoked nystagmus (GEN), consisting of centripetal DRT and centrifugal saccade with a mean saccadic amplitude of about 1° and a period in the range of 0.5-1.0 s. GEN is thought to be caused by defects in the oculomotor velocity-to-position integrator of the neural network within the brainstem and cerebellum. Patients with brainstem or cerebellar dysfunction present with significant GEN. However, recent studies suggest that even healthy subjects show weak GEN at a wide gaze angle, including small angles less than 30 °. At small angles, the weak GEN must be hidden in the FEyeM, but the details have not been studied. The FEyeM and GEN, which have been studied as separate phenomena, may be understood comprehensively. This thesis consists of two main parts: the experiment parts and the modeling parts. In the experiment part, this dissertation aimed to characterize the latent GEN in FEyeM during horizontal less-eccentric fixation and designed a simple experimental paradigm of gaze fixation at a target shifted horizontally from the front-facing position with less eccentricities. The dissertation separated the DRT and MS components from FEyeM and constructed the DRT and MS time series. The trend of DRT and MS was estimated as the slope of the regression line of the DRT and MS time series. Clear tendency of the centripetal DRT and the centrifugal MS as in the GEN, but with more stochasticity and with slower drift velocity compared to the GEN were found. The results showed that the target-shift-dependent balance between DRT and MS achieves the gaze bounded around each given target. In other words, the gaze relaxes slowly with the centripetal DRT toward the front-facing position during inter-MS intervals. A quasi-stable equilibrium posture always exists at the front-facing position, and MS actions pull the gaze intermittently back to the target position in the opposite direction of the DRT. In the modeling part, a neuromechanical model that has the potential to represent the slow DRT and stochastic MS characterized in the experiment part was constructed. This dissertation assumed that the eyeball is restricted to rotate only horizontally. Only two identical muscle models (corresponding to the lateral and medial rectus) are attached to each side of the eyeball. Their neural activities are emulated by the relaxation model with the MS firing threshold. The effort to bring the equilibrium position closer to the target position was important to reproduce the slowness of centripetal DRT in healthy people. This study will contribute to the comprehensive understanding of the control of the oculomotor system that cause FEyeM and GEN.

Contents

Chapter 1

Introduction

Human eyes always keep moving, even when one tries to fixate gaze (GZ) steadily. In this way, eyeball posture and the resultant GZ position fluctuate mostly involuntarily with small amplitudes during GZ fixation, referred to as fixational eye movement (FEyeM) (Ditchburn and Ginsborg, 1953; Rucci and Poletti, 2015), although recent studies report the voluntary aspects of FEyeM (Willeke et al., 2019). The corresponding time series of GZ position is referred to here as the GZ time series. It has been known that FEyeM contributes to visual perceptual constancy by counteracting sensory adaptation (Martinez-Conde et al., 2004). The GZ time series during FEyeM is composed of two types of eye movements: the drifts-tremor (DRT) and the microsaccade (MS). DRT is a slowly migrating quasi-continuous eye movement, like a Brownian motion, whose spectral power is dominated at a low-frequency band below 40 Hz, with the remaining power widely distributed in the range less than 100 Hz (Findlay, 1971; Ezenman et al., 1985). On the other hand, MS is a ballistic eye movement with a mean saccadic amplitude of about 0.3° during FEyeM (Martinez-Conde et al., 2009), which occurs approximately two times per second with Poisson-point-process-like inter-MS intervals (Cunitz and Steinman, 1969; Engbert and Kliegl, 2004; Engbert and Mergenthaler, 2006; Otero-Millan et al., 2008). When the GZ target is located at an eccentric position, typically with an eccentricity more than 30°, which forces one eyeball to rotate largely away from the nose and the other eyeball to rotate toward the nose, the GZ position, defined as the binocular eye position, exhibits oscillatory movements alternating between a centripetal drift toward the front-face position and a centrifugal saccade back to the fixation target position, with a mean saccadic amplitude of about 1° and the oscillation period in the range of 0.5 - 1.0 s. This phenomenon is known as the physiological gaze-evoked nystagmus (physiological GEN), also called end-point nystagmus (EPN). Recent studies suggested that healthy people commonly exhibit physiological GEN at wide horizontal angles of the fixation target, from − 40° to 40° across the entire range that humans can GZ (Whyte et al., 2010; Bertolini et al., 2013). On the other hand, dysfunctions of the brainstem or cerebellum can cause GZ instability, leading to pathological GEN (Cannon and Robinson, 1987; Versino et al., 1996). In both pathological and physiological GEN, the incidence rate of GEN and the absolute velocity of centripetal drifts increases with increasing GZ angle, i.e., high GZ eccentricity (Eizenman et al., 1990; B ü ttner and Grundei, 1995; Leigh and Zee, 2015; Tarnutzer et al., 2015). These studies imply that pathological GEN and physiological GEN share common neural networks within the cerebellum and the brainstem that has an oculomotor velocity-to-position neural integrator with leakiness. For example, increasing the amount of alcohol intake that impairs cerebellar oculomotor functions makes centripetal drifts faster with increased GZ eccentricity (Romano et al., 2017).

The relationships between FEyeM and physiological GEN have not been clearly understood. Bertolini et al. (2013) reported a linear relationship between a horizontal centripetal drift velocity of and horizontal GZ eccentricity (GZ angle of the fixation target) in healthy people, in which the slope of the linear relationship was about 0.02 [°/s]/[°], i.e., the horizontal centripetal drift velocity increases by the amount of 0.02/s per 1 of increase in the horizontal GZ eccentricity, for small GZ eccentricities less than 20°, and the slope was altered to about 0.05 [°/s]/[°] for large GZ eccentricities in the range of 20° to 40°. Their estimates imply a centripetal drift velocity of 0.2 °/s at a horizontal fixation point of 10°, which is non-negligibly large. To establish a GZ fixation with the error caused by such a non-negligible centripetal DRT velocity, the centrifugal MS must work for counterbalancing. However, because the fixation target used by Bertolini et al. was an LED that flashed briefly for 0.050 s every 2 s and moving between − 40° and 40° synchronously with the flashing, the FEyeM data acquired for each fixation point was too short to characterize the relationships between centripetal DRT and centrifugal MS in FEyeM in healthy people.

The purpose of this dissertation was to characterize centripetal DRT and centrifugal MS more accurately than previous studies as a function of the horizontal position with small GZ eccentricities, and to elucidate the counterbalanced coordination between centripetal DRT drift and centrifugal MS jumps. To this end, FEyeM in young healthy participants were measured to acquire the corresponding GZ time series for a small visual target presented in front of the face, and investigated how their characteristics change depending on the horizontal position of the target, particularly in the horizontal component of FEyeM. In the data analysis, the GZ time series were decomposed into DRT components and MS components to define the DRT time series consisting of DRT components only, as well as MS time series consisting of MS components only. Based on the DRT and MS time series, how they could be characterized differently depending on horizontal GZ position was investigated.

This dissertation is organized as follows and consists of Introduction, Experimental part (Characterization of Gaze Dynamics during Fixational Eye Movements at Small Gaze Eccentricities), Modeling part (Neuromechanical Modeling for Stochastic Gaze-evoked Nystagmus), General disccusion & conclusion, Appendix, and Publication. Each experimental part and modeling part has sub-chapters of methods, results, and discussion. This Chapter 1 shows introduction and explains about FEyeM (fixational eye movement), physiological GEN (Gaze-evoked nystagmus), the purpose of this study, and the construction of the thesis. The Chapter 2 is the experimental part about the characterization of gaze dynamics during fixational eye movements at small gaze eccentricities, which was reported in the international journal of Frontiers in Human Neuroscience [Ozawa et al., 2022]. The Chapter 3 is the modeling part about the neuromechanical model for stochastic gaze-evoked nystagmus, that is able to reproduce the characteristics of gaze dynamics during horizontal less-eccentric fixation. The Chapter 4 is the chapter of the general discussion and conclusion. In Appendix, the detailed mathematical explanations for the experimental part and modeling part were written. In Publication, journal papers, internatinoal conferences, and domestic conferences in which I participated as an author through the Ph.D course were listed. Journal papers, conference papers, and conferences with a notation of ”for reference only” mean that they have no direct relationship to this dissertation but were worked on through this Ph.D. course.

Chapter 2

Characterization of Gaze Dynamics During Fixational Eye Movements at Small Gaze Eccentricities

Involuntary eye movement during gaze (GZ) fixation, referred to as fixational eye movement (FEyeM), consists of two types of components: a Brownian motion like component called drifts-tremor (DRT) and a ballistic component called microsaccade (MS) with a mean saccadic amplitude of about 0.3° and a mean inter-MS interval of about 0.5 s. During GZ fixation in healthy people in an eccentric position, typically with an eccentricity more than 30°, eyes exhibit oscillatory movements alternating between centripetal drift and centrifugal saccade with a mean saccadic amplitude of about 1° and a period in the range of 0.5 - 1.0 s, which has been known as the physiological gaze-evoked nystagmus (GEN). Here, a simple experimental paradigm of GZ fixation on a target shifted horizontally from the front-facing position with fewer eccentricities was designed. The dissertation found a clear tendency of centripetal DRT and centrifugal MS as in GEN, but with more stochasticity and with slower drift velocity compared to GEN, even during FEyeM at GZ positions with small eccentricities. The results showed that the target shift-dependent balance between DRT and MS achieves the GZ bounded around each of the given targets. In other words, GZ relaxes slowly with the centripetal DRT toward the front-facing position during inter-MS intervals, as if there always exists a quasi-stable equilibrium posture in the front-facing position, and MS actions pull GZ intermittently back to the target position in the opposite direction to

DRT.

2.1 Materials and Methods

2.1.1 Measurements of FEyeM

2.1.1.1 Subjects

Eight healthy young adults (mean age 23.4, ranging from 22 to 25 years, all men) participated in the experiment. All subjects had normal or corrected to normal vision. They received monetary rewards (4,800 Japanese Yen) for their participation. The experiment was approved by the local ethics committee of Osaka University and was conducted under the Declaration of Helsinki. All participants gave written informed consent.

2.1.1.2 Experimental Systems

Binocular eye positions were obtained using a fast video-based eye movement monitor system (a dark pupil eye tracking system; iView X Hi-Speed, SensoMotoric Instruments, Teltow, Germany) with a sampling frequency of 500 Hz. A standard 13-point calibration was performed to align the eye and computer display coordinate systems. Subjects were seated in a chair in a black room, and their head was supported on a chin/forehead rest that included the support for the camera for eye tracking. A bite bar was also used for additional support for head fixation. A computer screen with a refresh rate of 120 Hz and an area of $1,920$ pixels $\times$ $1,080$ pixels for 0.524 m $\times$ 0.295 m width and height was placed 0.721 m from the eyes. The display was filled with a uniform white background of constant illumination (42.1 lux), regardless of the appearance and disappearance of the small visual target used in the task described below.

2.1.1.3 Experimental Protocol

To investigate the dependence of FEyeM on horizontal GZ direction, we prepared a small fixation target on the display at five locations that differed only in the horizontal direction (Figure 2.1.1A). The target was persistently located at 0 in the vertical direction, and at -15.2°, -7.76°, 0°, 7.76°, and 15.2° in the horizontal direction. Five target locations (conditions) from the left to right were referred to as L2, L1, C, R1, and R2, respectively. We measured FEyeM to acquire the corresponding GZ time series for those five locations of the fixation target. The fixation target was a small black square with a size of 7 pixels $\times$ 7 pixels (0.15°). The target location was randomly chosen and presented to each subject. Subjects were informed that the fixation target appeared somewhere in the horizontal position at the vertical center of the display, and were asked to fixate on the target while it appeared as accurately as possible. Subjects were allowed to blink freely during the fixation task. One session was composed of seven fixation trials. Each single trial lasted 35 s, which was interrupted by several eye blinks, for a fixed target position that was chosen pseudorandomly from the five positions. Each subject performed eight sessions, i.e., 56 trials in total on a single experimental day. A pseudorandom sequence of 56 target positions used in 56 trials for the eight sessions was predetermined, in which the randomness was manipulated so that each of the four positions was chosen 11 times and the remaining one position was chosen 12 times. We provided a break of 10 s between trials and of 10 - 30 min rest between sessions. Data acquisition for each subject lasted for 4 h. The schematic view of the experimental protocol is shown in Figure 2.1.1B.

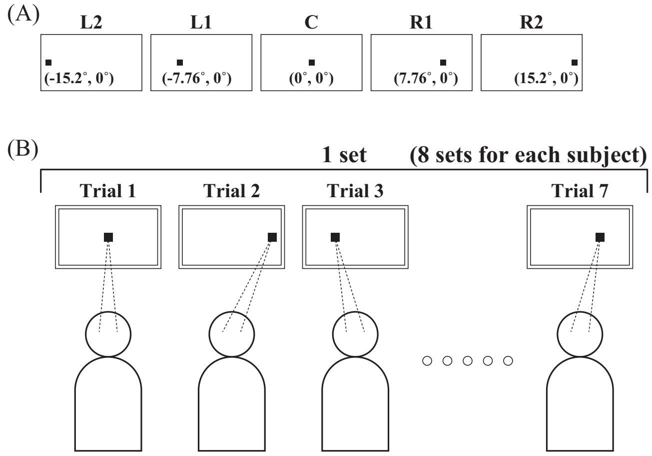

Figure 2.1.1: Schematic diagram of the experiment. (A) Five target positions from the left to right, which were referred to as L2, L1, C, R1, and R2, respectively. (B) The experimental protocol. A small target was projected at 0° in the vertical direction and at -15.2°, -7.76°, 0°, 7.76°, and 15.2° in the horizontal direction. Fixational eye movements (FEyeM) were measured to obtain gaze (GZ) time series for each of those five positions of the fixation target. Single trial lasted for 35 s, which was interrupted by several eye blinks. A target position for each trial was chosen pseudo-randomly from the five locations. Each subject performed 56 trials in total.

2.1.2 Data Analysis

2.1.2.1 Preprocessing

The first and last 2.5-s segments of the GZ time series of each trial were removed to avoid possible effects of the initial transient and the expectation of the end of the trial.

Blinks were detected by referring to the known properties of blinks (Caffier et al., 2003), automatically for complete blinks and manually with visual inspections for incomplete blinks. For automatic detection, the onset and offset of each blink were detected based on the vertical pupil diameter, where a value of 2/3 of the mean diameter of each GZ series was used as the threshold for detecting the onset and offset of each blink. We removed a 1.0-s long segment of the GZ time series, as a blink segment, from the pre-blink time of 0.22 s (± 0.074 s) before onset to the post-blink time of 0.53 s (± 0.18 s) after offset. Pre-blink and post-blink intervals were determined such that the sum of pre-blink, post-blink, and blink intervals was 1.0 s, and the ratio between pre-blink and post-blink intervals was 1 : 2.4. By removing the data segments during the detected blinks, the GZ series of each trial was divided into short segments corresponding to the inter-blink intervals. Each of the short segments obtained represents a sample path of the GZ time series. We excluded data segments (typically corresponding to very short inter-blink interval cases) that did not contain any MS events that were identified by the method described below. In this study, we focused on the binocular aspects of FEyeM only in the horizontal direction. Thus, we computed the average time series of the left and right GZ positions in the horizontal direction for further analysis. Note that, the version components are emphasized through the averaging of the left and right GZ time series, because the vergence components cancel and would be almost absent from the averaged binocular GZ time series. Note also that the version position was defined as the average between the left and right eye positions, as in previous studies (Collewijn et al., 1997; Quinet et al., 2020). Because the center of the GZ direction is not decided by the dominant eye, but is located between the two eyes as the cyclopean eye (Ono and Barbeito, 1982), the average binocular GZ values approximate the center of the GZ direction. In this way, any GZ time series hereafter for further analysis was redefined as the binocular GZ time series averaged for an inter-blink interval.

2.1.2.2 Decomposing GZ Time Series Into DRT and MS Series

A GZ time series can be decomposed into DRT components and MS components using an algorithm summarized here (see the Supplementary Material for a detailed mathematical description of the algorithm). After decomposition, we analyzed DRT and MS components of the GZ time series separately. To this end, we defined the DRT time series $X_{\mathrm{DRT}}(t)$ and the MS time series $X_{\mathrm{MS}}(t)$ consisting of only DRT and MS components, respectively, for a given GZ time series that was referred to as the raw gaze (raw-GZ) time series $X_{\mathrm{rGZ}}(t)$, where t represents the discrete time of the data with a sampling time interval of $\delta_s = 0.002$ s. Figure 2 shows a representative example of the experimental time series $X_{\mathrm{DRT}}(t)$ and $X_{\mathrm{MS}}(t)$ with the corresponding $X_{\mathrm{rGZ}}(t)$. The origins (0) of those time series represented the front-facing position of the GZ, and the right and left directions for the subject were defined as the positive and negative values of the GZ positions. We defined the MS time series $X_{\mathrm{MS}}(t)$ by eliminating overshoot components as well as a ballistic transient component of each MS from the raw-MS time series (Ozawa and Nomura, 2019), and analyzed it for making relationships between DRT and MS clear, because we were not interested in the detailed temporal structure of each MS waveform. Note that an overshoot is a small overrun component that is followed by a small return in the opposite direction to MS immediately after MS, after which the GZ position settles at the beginning of subsequent DRT motion. In other words, the MS time series $X_{\mathrm{MS}}(t)$ was obtained by replacing each transient ballistic component plus overshoot of MS in the raw-MS time series by an instantaneous jump in amplitude determined by the onset and offset of MS from the raw-MS time series [see Equation (2.1.3)]. Using $X_{\mathrm{MS}}(t)$, we defined the simplified GZ time series $X_{\mathrm{GZ}}(t)$, referred to simply as the GZ time series in this sequel. In this study, we would show that each of $X_{\mathrm{DRT}}(t)$ and $X_{\mathrm{MS}}(t)$ exhibited a unidirectional linear trend that diffuses in the opposite direction to each other, and the slopes of their linear trend altered depending on the degree of small eccentricity of the horizontal fixation position, i.e., L2, L1, C, R1, and R2. To this end, we characterized such trends in $X_{\mathrm{DRT}}(t)$ and $X_{\mathrm{MS}}(t)$, and the variation of $X_{\mathrm{GZ}}(t)$ as the sum of those two types of time series. In particular, we quantified the slopes of the linear trend of $X_{\mathrm{DRT}}(t)$ and $X_{\mathrm{MS}}(t)$ by the least-squares linear regression of $X_{\mathrm{DRT}}(t)$ and $X_{\mathrm{MS}}(t)$, denoted by $\mu_{\mathrm{DRT},k}$ and $\mu_{\mathrm{MS},k}$, respectively, for the kth sample path. Then, subject-wise mean values of the slopes, denoted $\hat{\mu}_{\mathrm{DRT}}$ and $\hat{\mu}_{\mathrm{MS}}$, were computed for each target position. The mean slope values across the eight subjects were summarized as boxplots for L2, L1, C, R1, and R2 to elucidate how the $\hat{\mu}_{\mathrm{DRT}}$ and $\hat{\mu}_{\mathrm{MS}}$ altered depending on the degree of eccentricity of the horizontal fixation point.

2.1.2.3 Random-Walk Analysis of GZ and DRT Time Series

The diffusion properties of $X_{\mathrm{DRT}}(t)$ and $X_{\mathrm{GZ}}(t)$ were characterized by the mean squared displacements (MSD) as functions of the time lag $\tau \cdot \delta_s$ defined as follows:

$$\langle (\Delta x_{\mathrm{GZ}}(\tau))^2 \rangle = \frac{1}{N-\tau} \sum_{j=1}^{N-\tau} \left| x_{\mathrm{GZ}}(j+\tau) - x_{\mathrm{GZ}}(j) \right|^2, \tag{2.1.1}$$

$$\langle (\Delta x_{\mathrm{DRT}}(\tau))^2 \rangle = \frac{1}{N-\tau} \sum_{j=1}^{N-\tau} \left| x_{\mathrm{DRT}}(j+\tau) - x_{\mathrm{DRT}}(j) \right|^2, \tag{2.1.2}$$

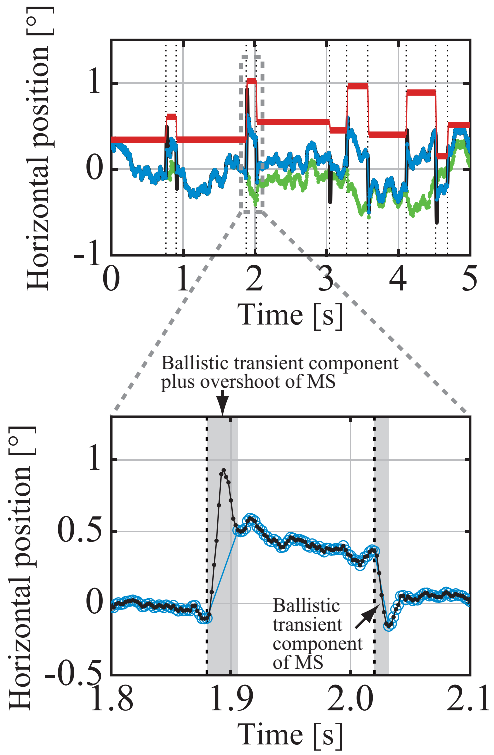

Figure 2.1.2: A representative example of the raw-GZ time series $X_{\mathrm{rGZ}}(t)$ (black curve, mostly behind the blue curve), the GZ time series $X_{\mathrm{GZ}}(t)$ (blue curve), which was decomposed into the DRT time series $X_{\mathrm{DRT}}(t)$ (green curve), and the MS time series $X_{\mathrm{MS}}(t)$ (red line). The vertical dotted lines indicate the time instants when MS events (MS onset and offset) occurred. The enlarged view compares the details of the raw-GZ time series $X_{\mathrm{rGZ}}(t)$ (small black filled circles) with ballistic transient and overshoot components of two MS events and the GZ time series $X_{\mathrm{GZ}}(t)$ (blue open circles). Ballistic transient and overshoot components were eliminated from the raw-GZ to obtain the GZ time series.

where N is the total number of data included in the time interval of T_{GZ} for a given sample path. Note that MSD is also known as the stabilogram diffusion analysis (Collins and De Luca, 1993; Engbert and Kliegl, 2004). Double-log plots of MSD as a function of τ for each target position were obtained by performing an ensemble average over all sample paths for each subject. From the estimated MSD scaling exponent, we characterized the degree of diffusion of $X_{\mathrm{DRT}}(t)$ and $X_{\mathrm{GZ}}(t)$ in comparison with the Brownian motion that exhibits the unit scaling exponent (which is equal to $2H$ for the Hurst exponent H) with its variance determined as the averaged variance of the increment per second of the DRT time series.

2.1.2.4 Detection and Simplification of MS

We detected MS events using the method of Engbert and Kliegl, referred to as the E&K method (Engbert, 2006) as illustrated in Figure 2.1.3. In the E&K method, a parameter λ was introduced to determine the velocity ellipse size in the vx-vy plane, where v_x and v_y were the velocities of the GZ motion in the horizontal and vertical directions, respectively [see Engbert and Kliegl (Engbert, 2006) for the definition of the parameter λ]. In this study, we used $\lambda = 7$ for all target position conditions. Some MS events acquired from eye movements measured by a pupil-based eye tracking system and detected by the E&K method might contain overestimated overshoot components (Otero-Millan et al., 2014; Nyström et al., 2016; Ozawa and Nomura, 2019). The validity of the MS events detected by the E&K method in the current study was confirmed by drawing the main sequence diagrams for the MS events (see Figure A1 in Appendix).

As mentioned above, the MS time series $X_{\text{MS}}(t)$ for the analysis were obtained by replacing each transient trajectory plus the overshoot component of MS in the raw-MS time series $X_{\text{rMS}}(t)$ with an instantaneous jump (see Figures 2.1.2, 2.1.3). More specifically, for an onset time of the ith MS of the kth sample path of the raw-MS series, denoted by $X_{\text{rMS},k}(t)$, occurred at t^i_{on} and the corresponding offset time at t^i_{off}, the amplitude of the ith MS (size of the instantaneous jump) was defined as

$$w_{i,k} = X_{\text{rMS},k}(t^i_{off}) - X_{\text{rMS},k}(t^i_{on}) \tag{2.1.3}$$

where$t^i_{on} \cdot \delta_s$ and $t^i_{off} \cdot \delta_s$ were the time instances when GZ velocity trajectory in the v_x-v_y plane cut the velocity ellipse of the E&K method from inside to outside and from outside to inside, respectively. Note that, in $X_{\text{MS}}(t)$, any MS occurs in unit time step, because transient plus overshoot portions of the corresponding MS in XrMS(t) were eliminated by the definition of $X_{\text{MS}}(t)$. Positive and negative amplitudes $w_{i,k}$ for the ith MS in the kth sampling path means that the corresponding MS jumps to the right and left, respectively, and their absolute value represents the jump size. The rightward and leftward MS events in the kth sampling path were counted separately when necessary, by which the signed amplitude of the ith rightward MS and the jth leftward MS were denoted, respectively, by $w_{+,i,k}$, $w_{-,j,k}$. The total number of rightward and leftward MS events in the kth sampling path were denoted by $n_{+,k}$ and $n_{-,k}$, respectively. The subject-wise means of $w_{i,k}$, regardless of the jump direction, as well as the subject-wise means of $w_{+,i,k}$ and $w_{-,j,k}$, across all sampling paths were computed and denoted by $\hat{w}$, $\hat{w}_+$, and $\hat{w}_-$, respectively.

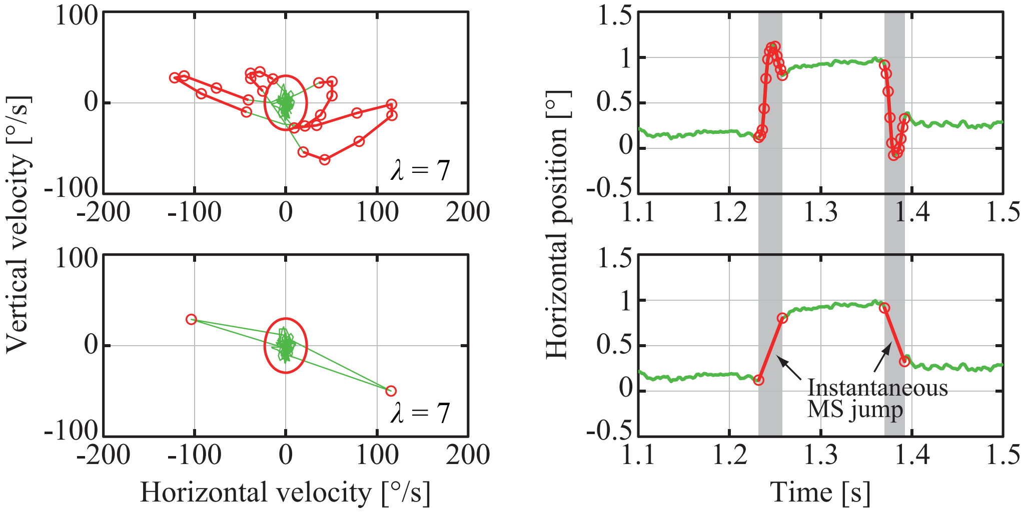

Figure 2.1.3: Detection and simplification of MS events. The upper panels show an example of raw-GZ data with an MS event detected by the Engbert and Kliegl (E&K) method in the v_x-v_y plane (left panel) and the corresponding time profile (right panel), where the red curves are MS components and the green curves are DRT components. The lower panels are for the corresponding GZ data, in which MS events were simplified, referred to simply as MS in this paper, by eliminating the transient and overshoot ballistic components from the raw-MS waveforms for further analysis performed in this paper.

2.1.2.5 Temporal Structure of MS Time Series

The temporal structure of the MS time series was characterized by the histogram of the inter-microsaccadic intervals (IMSI) in the right and left directions. Because the probability of the occurrence of MS events has been approximated by a Poisson-point-process (Engbert, 2006), for which the IMSI obeys the exponential distribution with the exponential probability density function (PDF), we approximated the histograms of IMSI in each of the rightward (+) and leftward (−) directions by

$$p(x; \lambda_{\pm}) = \lambda_{\pm} e^{-\lambda_{\pm} x} \tag{2.1.4}$$

for IMSI values $x = \mathrm{IMSI}_+$ between subsequent rightward MS events with occurrence frequency λ_+ and for $x = \mathrm{IMSI}_-$ between subsequent leftward MS events with occurrence frequency λ_-. For the kth sample path of $X_{\mathrm{GZ}}(t)$ with the data length (the inter-blink interval) $T_{\mathrm{GZ},k}$, the estimates of the Poisson rates λ_+ and λ_-, denoted, respectively, by $\Lambda_{+,k}$ and $\Lambda_{-,k}$, were obtained as the inverse of the mean MS interval, i.e.,

$$\Lambda_{+,k} = \frac{n_{+,k}}{T_{\mathrm{GZ},k}}, \Lambda_{-,k} = \frac{n_{-,k}}{T_{\mathrm{GZ},k}} \tag{2.1.5}$$

where $n_{+,k}$ and $n_{-,k}$ were the numbers of rightward and leftward MS events, respectively. Moreover, we also computed the occurrence frequency of the total number of MS events, regardless of the direction of the jumps, as

$$\Lambda_k = \frac{n_{+,k} + n_{-,k}}{T_{\mathrm{GZ},k}} \tag{2.1.6}$$

for the kth sample path. For those MS rate parameters, the subject-wise mean values, i.e., $\hat{\Lambda}_+$, $\hat{\Lambda}_-$, and $\hat{\Lambda}$, were computed. In addition to those estimates of MS occurrence, the slopes of the least-squares linear regression lines for semi-log plots of the IMSI$_+$ and IMSI$_-$ histograms were performed, by which alternative estimates of the Poisson rates for each subject, denoted by $\hat{\lambda}_+$ and $\hat{\lambda}_-$, respectively, were obtained, which should be consistent with the $\hat{\Lambda}_+$ and $\hat{\Lambda}_-$ obtained by Equation 2.1.5, if the occurrence of each of the rightward and the leftward MS events obeyed the Poisson-point-process. The consistency between $\hat{\Lambda}_\pm$ and $\hat{\lambda}_\pm$ confirms the assumption of the Poisson-point-process property of the MS events.

As described above, the unidirectional linear trend of the MS time series $X_{\mathrm{MS}}(t)$ for the kth sample path was quantified by the slope $\mu_{\mathrm{MS},k}$ of the least-squares regression line. We computed the subject-wise mean values of $\mu_{\mathrm{MS},k}$, denoted by $\hat{\mu}_{\mathrm{MS}}$. Alternatively, the linear trend of the stair-like MS time series for the kth sample path could be quantified using the mean jump sizes $\hat{w}_{+,k} > 0$ and $\hat{w}_{-,k} < 0$ and their mean occurrence frequency per second by introducing the parameter s_k defined as follows:

$$s_k \triangleq w_{+,k}\lambda_{+,k} + w_{-,k}\lambda_{-,k}. \tag{2.1.7}$$

Then, $\hat{s}$ as the subject-wise mean of s_k across all trials for each subject was also computed. Comparisons between those two types of quantifications, i.e., $\hat{\mu}_{\mathrm{MS}}$ and $\hat{s}$ across subjects were made to elucidate the underlying mechanisms of the unidirectional linear MS trend as well as the DRT time series. Specifically, to elucidate the dominant contributing parameters, among $\hat{\lambda}_+$, $\hat{\lambda}_-$, $\hat{w}_+$, and $\hat{w}_-$, that characterize the temporal structure of the MS time series to the unidirectional linear trend of the MS time series, we compared the means of those four parameters across all subjects using boxplots of the parameters for the five fixation conditions, i.e., L2, L1, C, R1, and R2. Furthermore, the boxplots of the values of $\hat{s}$ across all subjects for the five fixation conditions were examined, which were compared with the boxplots of the slope $\hat{\mu}_{\mathrm{MS}}$ of the least-squares linear regression line, to show that an appropriately biased balance of the rates and amplitudes between rightward and leftward MS events was the major cause of the unidirectional linear trend of the MS time series. The comparisons between $\hat{\lambda}_+$ and $\hat{\lambda}_-$ and between $\hat{w}_+$ and $\hat{w}_-$ for each of the five target positions were also performed to examine the differences between rightward and leftward MS jumps.

2.1.2.6 Relationships Between Onset Position of MS and Amplitude With Direction of MS

The relationships between the onset position of MS and its amplitude were analyzed by examining their joint PDF, for which the corresponding two-dimensional histograms of the onset position and amplitude of MS with 0.25° and 0.20° bin widths were calculated, respectively. Then, cubic spline interpolation of the histogram between the bins (meshes), which was displayed as a color map of the joint frequency of the onset positions and amplitudes of the MS events, was performed. Moreover, to investigate the relationships between the onset position and the jump direction of MS, a one-dimensional histogram with a bin width of 0.10° was calculated for each of the rightward and leftward MS events. To investigate the MS amplitude distribution, a one-dimensional histogram with a bin width of 0.10° was calculated for each of the rightward and leftward MS events. For supplementary information, a one-dimensional histogram of the GZ time series for each fixation condition was calculated, corresponding to the PDF of the GZ time series, which was shown below the color map.

2.1.2.7 Examining the Balance Between the Linear Trends of DRT and MS

The dissertation hypothesized that the GZ fixation for each of the five target positions was established by the balance between the unidirectional linear trends of the DRT and MS time series in opposite directions. To examine such a balance, scatter plots for s_k defined by Equation (2.1.7) against the unidirectional linear trend of DRT $\mu_{\mathrm{DRT},k}$ for all sample paths k across all subjects were examined. Negative correlation with the slope of minus one in the scatter plot implies that the centripetal DRT and the centrifugal MS are completely balanced, as in the following equation

$$\mu_{\mathrm{DRT}} = -s. \tag{2.1.8}$$

Moreover, the means of $\mu_{\mathrm{DRT},k}$ and the parameter s_k were calculated for all kth sample paths across all subjects, denoted by $\bar{\mu}_{\mathrm{DRT}}$ and s, respectively, for each target position, which were indicated on the scatter plots.

2.1.2.8 Target Position Dependent Basic Properties of FEyeM

To characterize target position-dependent basic properties of FEyeM, other than the direct drift-related properties, statistical mean values of the following 14 metrics for the GZ time series $X_{\mathrm{GZ}}(t)$, averaged across all trials (all sample paths) and all subjects for each target position were calculated: the data length T_{GZ} of $X_{\mathrm{GZ}}(t)$ defined by 15 supplementary equations in the Appendix A that represents the inter-blink interval, the time average of GZ position $X_{\mathrm{GZ}}(t)$, the standard deviation (SD) of $X_{\mathrm{GZ}}(t)$, the absolute error between the target position and the GZ position, the amplitude of the total MS regardless of the direction, and the rightward MS and the leftward MS (i.e., $\hat{w}$, $\hat{w}_+$, and $\hat{w}_-$ as defined above), the occurrence frequency $\hat{\Lambda}$ for the total MS regardless of the direction using Equation (2.1.6), and the occurrence frequencies of the rightward and leftward MS events by $\hat{\Lambda}_+$ and $\hat{\Lambda}_-$ from Equation (2.1.5) as well as by$\hat{\lambda}_+$ and $\hat{\lambda}_-$ based on the exponential fitting of IMSI histograms, the onset position of MS relative to the mean GZ position, and the offset position of MS relative to the mean GZ position.

2.1.2.9 Statistical Analysis

To examine the target position dependence on any metrics characterizing the GZ, DRT, and MS time series, Bartlett's test to examine the equality of variances among five target positions (L2, L1, C, R1, and R2) was performed and confirmed at the 5% significance level. The Tukey - Kramer test was then performed to examine the differences between them at the 5 and 1% significance levels.

2.2 Results

2.2.1 Basic Statistics

Table 2.2.1 shows the dependence of horizontal GZ position on the mean values of 14 metrics averaged across all subjects. There were no significant differences between horizontal GZ positions in the following 12 metrics: mean values of the data length T_{GZ} of $X_{\mathrm{GZ}}(t)$, the GZ position, the SD of the GZ position, absolute value of the error from the target, amplitude of the rightward and the leftward MS events ($\hat{w}_+$ and $\hat{w}_-$), occurrence frequency of the rightward and the leftward MS events ($\hat{\Lambda}_+$ and $\hat{\Lambda}_-$ as well as $\hat{\lambda}_+$ and $\hat{\lambda}_-$), occurrence frequency of the total MS events $\hat{\Lambda}$, and the relative onset position of MS. Significant differences ($p < 0.05$) were found only in the amplitude $\hat{w}$ of total MS and relative MS offset position between L2 and R2. However, the SD of the GZ position and absolute error from the target tended to be large as the eccentricity was increased, although without no statistical significance.

Table 2.2.1: Dependence of horizontal gaze (GZ) position on the mean of each statistic for all subjects.

Mean Values across 8 Subjects	Horizontal Fixation Target				
	L2	L1	C	R1	R2
Data Length, T_{GZ} [s]	15.6(±8.08)	16.1(±8.57)	16.7(±8.78)	15.2(±6.68)	14.5(±8.40)
Gaze Position, X_{GZ} [°]	−15.2(±0.215)	−7.79(±0.131)	0.0236(±0.158)	7.77(±0.121)	15.1(±0.219)
SD of Gaze Position [°]	0.246(±0.0406)	0.230(±0.0250)	0.206(±0.0152)	0.228(±0.0354)	0.243(±0.0271)
Absolute Error from Target [°]	0.363(±0.0977)	0.299(±0.117)	0.271(±0.0743)	0.319(±0.161)	0.347(±0.0773)
Amplitude of Total MS, $\hat{w}$ [°]*	−0.0514(±0.0622)	−0.0258(±0.0459)	0.0016(±0.0370)	0.0164(±0.0372)	0.0392(±0.0532)
Amplitude of Leftward MS, $\hat{w}_-$ [°]	−0.363(±0.132)	−0.361(±0.0996)	−0.314(±0.0875)	−0.315(±0.103)	−0.326(±0.105)
Amplitude of Rightward MS, $\hat{w}_+$ [°]	0.354(±0.105)	0.348(±0.0842)	0.310(±0.0763)	0.329(±0.0867)	0.354(±0.112)
Frequency of Total MS, $\hat{\Lambda}$ [1/s]	1.66(±0.499)	1.55(±0.478)	1.47(±0.560)	1.57(±0.544)	1.67(±0.512)
Frequency of Leftward MS, $\hat{\Lambda}_-$ [1/s]	0.934(±0.274)	0.842(±0.291)	0.745(±0.312)	0.803(±0.333)	0.818(±0.287)
Frequency of Rightward MS, $\hat{\Lambda}_+$ [1/s]	0.738(±0.250)	0.727(±0.216)	0.745(±0.263)	0.779(±0.206)	0.891(±0.209)
Frequency of Leftward MS, $\hat{\lambda}_-$ [1/s]	1.21(±0.374)	1.07(±0.325)	0.967(±0.411)	1.09(±0.386)	1.02(±0.423)
Frequency of Rightward MS, $\hat{\lambda}_+$ [1/s]	0.854(±0.462)	0.966(±0.395)	0.902(±0.367)	1.02(±0.335)	1.12(±0.322)
Relative Onset Position of MS to Mean Gaze Position [°]	0.024(±0.050)	0.018(±0.050)	0.0044(±0.032)	−0.001(±0.018)	−0.0052(±0.0031)
Relative Offset Position of MS to Mean Gaze Position [°]*	−0.040(±0.054)	−0.014(±0.046)	0.0053(±0.032)	0.019(±0.032)	0.042(±0.043)

2.2.2 GZ, DRT, and MS Time Series

The upper panels of Figure 2.2.1 show all sample paths of the GZ time series $X_{\mathrm{GZ}}(t)$, DRT time series $X_{\mathrm{DRT}}(t)$, and MS time series $X_{\mathrm{MS}}(t)$, for a representative subject. The least-squares linear regression line was superimposed on each of $X_{\mathrm{GZ}}(t)$, $X_{\mathrm{DRT}}(t)$ and $X_{\mathrm{MS}}(t)$ for each of the five fixation targets. For $X_{\mathrm{GZ}}(t)$, the blue time series in the upper left panel of Figure 2.2.1, we could observe the time series fluctuating around the target position. Together with the fact that the SD of $X_{\mathrm{GZ}}(t)$ and the absolute error were small, as shown in Table 2.2.1, with no dependence on target position, it was confirmed that the GZ fixation was performed correctly, regardless of the horizontal target position. For $X_{\mathrm{DRT}}(t)$, the green time series in the upper middle panel of Figure 2.2.1 , the unidirectional linear trend toward the front-facing position (i.e., the horizontal center at 0°) was found for the target position of L2, L1, R1, and R2. That is, $X_{\mathrm{DRT}}(t)$ exhibited the centripetal drift. On the other hand, in the upper right panel of Figure 2.2.1 , the red time series of $X_{\mathrm{MS}}(t)$ showed the unidirectional linear trend in the opposite direction to DRT, i.e., away from the front-facing position, were found for the target position of L2, L1, R1, and R2. In other words, $X_{\mathrm{MS}}(t)$ exhibited a centrifugal trend. The linear trend of each time series was quantified by the slope of the least-squares linear regression line, and the mean slope averaged across all subjects for each of the five target positions as depicted in the lower panels of Figure 2.2.1 . The slopes of $X_{\mathrm{GZ}}(t)$ were close to 0 for all of the five target positions, and there were no significant differences in the slopes of $X_{\mathrm{GZ}}(t)$ among the five target positions. That is, GZ fixation was performed correctly regardless of the fixation position. On the other hand, in the $X_{\mathrm{DRT}}(t)$ and $X_{\mathrm{MS}}(t)$ boxplots, the slope became steeper as the target GZ angle became larger, in the opposite direction from each other. That is, the centripetal drift of $X_{\mathrm{DRT}}(t)$ and the centrifugal trend of $X_{\mathrm{MS}}(t)$ became faster as the target GZ angle increased. The differences between the slopes were significant between L2 and R2 ($p < 0.01$), between L2 and R1 ($p < 0.05$), and between L1 and R2 ($p < 0.05$) for both of $X_{\mathrm{DRT}}(t)$ and $X_{\mathrm{MS}}(t)$. For the L2 and R2 conditions, the mean absolute values of the linear trend of $X_{\mathrm{DRT}}(t)$ and $X_{\mathrm{MS}}(t)$ were about 0.1°/s. Note that there were some subjects who did not exhibit the target position-dependent linear trends of $X_{\mathrm{DRT}}(t)$ and $X_{\mathrm{MS}}(t)$.

2.2.3 Random-Walk Analysis

Figure. 2.2.2 shows the MSD of $X_{\mathrm{GZ}}(t)$ and $X_{\mathrm{DRT}}(t)$ for a representative subject for each of the five target positions. Over a wide range of time lag (0.002 - 10 s), regardless of the horizontal fixation condition, the scaling exponent of the DRT time series, which corresponds to $2H$ for the Hurst exponent H, was about 1, i.e., $H \sim 1/2$. That is, the

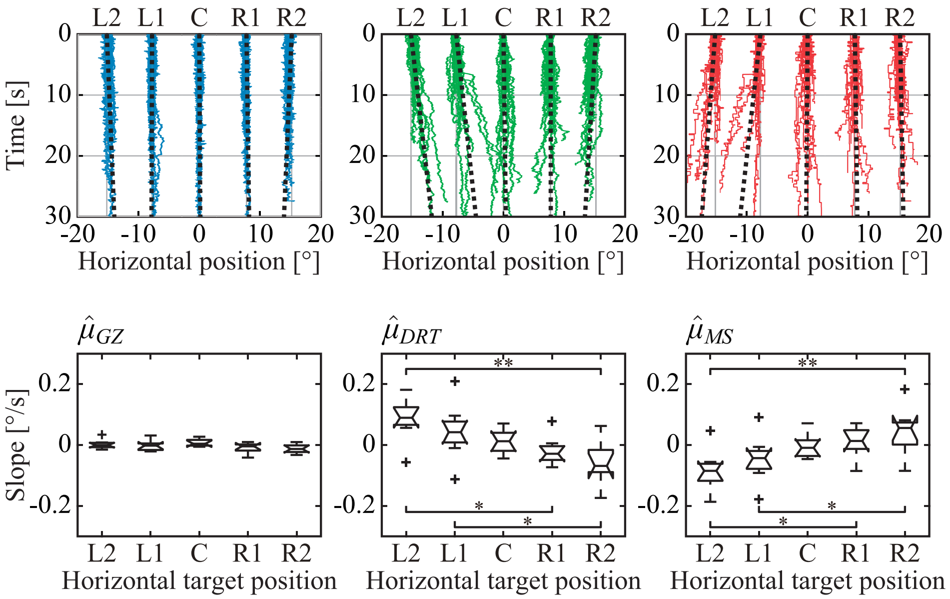

Figure 2.2.1: Horizontal dependence of the target position on GZ, DRT, and MS time series and the slopes on their trend. Upper panels: All sample paths of GZ (left, blue), DRT (middle, green), and MS (right, red) time series of a representative subject were superimposed for each of the five target positions. Black dotted lines are the least-squares linear regression lines, representing the linear trend of the time series for each of the five target positions. Lower panels: box plots of the mean value of the subject-wise means of slopes for each time series across all subjects. Single and double asterisks indicate that there was a significant difference between groups at the 5 and 1% significance level, respectively.

MSD profile of the DRT time series was similar to the MSD of the Brownian motion, regardless of the target position, despite of the fact that the slope (i.e., the velocity) of the centripetal linear trend of the DRT time series exhibited a clear dependence on the target position. This means that the centripetal DRT linear trend was not caused by a positive persistence of the DRT time series (see Section Discussion). On the other hand, the MSD of the GZ time series $X_{\text{GZ}}(t)$ exhibited a crossover phenomenon, in which the critical point (critical time lag) was located around 0.1 - 0.2 s. The $2H$ scaling exponent of $X_{\text{GZ}}(t)$ for the short-time scale (0.002 - 0.1 s) was about 1, whereas that for the long-time scale (0.2 - 10 s) was between 0.1 and 0.3, regardless of the target position. In summary, the MSD of $X_{\text{GZ}}(t)$ and $X_{\text{DRT}}(t)$, i.e., the random-walk property of the GZ and DRT time series did not show the dependence on the target position, despite the fact that the slope (i.e., the velocity) of the centripetal linear trend of the DRT time series and the centrifugal linear trend of the MS time series exhibited a clear dependence on the target position.

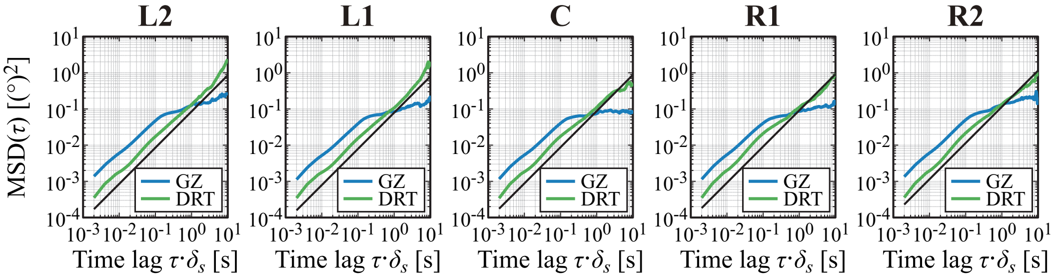

Figure 2.2.2: Mean square displacement (MSD) analysis of the GZ and DRT time series. The blue and green curves represent, respectively, the MSDs of the GZ and DRT time series. The black lines are the MSD of the Brownian motion for comparison. The MSD curves depicted in each panel are the ensemble average of MSD for each sample path of a representative subject.

2.2.4 Characterization of MS Time Series

Detailed characterizations of the MS time series are presented in Figures 2.2.3, 2.2.4 for a representative subject and in Figure 2.2.5 obtained using data from all subjects. Regardless of the target position, a negative correlation between MS onset position and amplitude ($\hat{w}_+$ and $\hat{w}_-$) was found, as represented in each panel of Figure 2.2.3. More specifically, the onset positions were localized at locations about 0.3° from the average GZ position, in both the negative (left) and the positive (right) directions, from which MS with an amplitude of about 0.3° occurred in the positive (rightward) and the negative (leftward) directions, respectively, regardless of the target position. The histograms of MS events tended to be more horizontally stretched and became asymmetric as the target position was more distant from the front-facing position. For the target positions on the left, particularly for the L2 condition, the peaks of the histograms (in the upper side of the color maps) for the leftward MS (the blue histograms) were slightly higher than those for the rightward MS (the red histograms). Moreover, the mean value of the MS onset (the dashed vertical black line in the color map) was slightly shifted to the right from the target position (the dash-dot vertical white line). In contrast, for the target positions on the right, particularly for the R2 condition, the peaks of the rightward MS histograms (the red histograms) were slightly higher than those of the leftward MS histograms (the blue histograms). Moreover, the mean value of the MS onset (the dashed vertical black line in the color map) was slightly shifted to the left from the target position (the dash-dot vertical white line). In this way, MS events occurred more frequently toward the centrifugal direction compared to the centripetal direction. However, these differences between rightward and leftward MS events were not statistically significant, as shown in Table 2.2.1.

It was confirmed in Figure 2.2.4 that the occurrence probability of IMSI with both in the positive (IMSI_+) and negative (IMSI_-) directions obeyed the exponential distribution with the identical rate parameter, regardless of the target position (see Table 2.2.1 for a comparison of the rates $\hat{\lambda}_+$ and $\hat{\lambda}_-$). Figure 2.2.5 shows the boxplots of $\hat{s}$ as the mean of the subject-wise mean values of $s_k \triangleq w_{+,k}\lambda_{+,k}+w_{-,k}\lambda_{-,k}$, as well as $\hat{\lambda}_+$,$\hat{\lambda}_-$, $\hat{w}_+$ and $\hat{w}_-$ that characterize the target position dependency of the occurrence frequency and the amplitude of MS for each of the five target positions. The top panel of Figure 2.2.5 shows that $\hat{s}$, representing the velocity of centrifugal trend of $X_{\mathrm{MS}}(t)$, increased linearly from negative to positive values as the target location varied from the left to the right. This dependency was apparent and quantitatively the same as the target position dependency of the mean slope of the regression lines for the centrifugal linear tend of $X_{\mathrm{MS}}(t)$ (the lower right panel of Figure 2.2.1), which counterbalanced with the opposite dependency of the mean slope of the regression line for the centripetal linear trend of $X_{\mathrm{DRT}}(t)$ (the lower middle panel of Figure 2.2.1). Specifically, differences in $\hat{s}$ were significant between L2 and R2 ($p < 0.01$), and between L2 and R1 ($p < 0.05$). As described for the asymmetric shape of the histograms in Figure 2.2.3, the occurrence frequencies of the rightward $\hat{\lambda}_+$ and leftward $\hat{\lambda}_-$ MS events slightly increased and decreased, respectively, as the target position varied from the left to the right (the middle row panels of Figure 2.2.5), although the pairwise comparison between those values for the five target positions were not different significantly (Table 2.2.1). The values of $\hat{\lambda}_+$ and $\hat{\lambda}_-$ for each target position were also compared, because it seemed $\hat{\lambda}_+ < \hat{\lambda}_-$ for L2 and $\hat{\lambda}_+ > \hat{\lambda}_-$ for R2 by the visual inspection. However, the differences between the rates of rightward and leftward MS events within the same target position were not statistically significant. Moreover, there was no recognizable nor statistically significant target position dependency in the amplitude of the leftward $\hat{w}_-$ and rightward $\hat{w}_+$ MS events (the middle row panels of Figure 2.2.5). In any cases, each of the parameters $\hat{\lambda}_+$, $\hat{\lambda}_-$, $\hat{w}_+$, and $\hat{w}_-$ alone did not show significant dependency on the target position.

2.2.5 Balance Between the Unidirectional Trends of the DRT and MS Time Series

The linear trend of DRT quantified by the slope of the least-squares linear regression line $\mu_{\mathrm{DRT},k}$ and the linear trend of MS quantified by s_k defined by Equation (2.1.7) for the kth sample path were compared by the scatter plot for each target position across

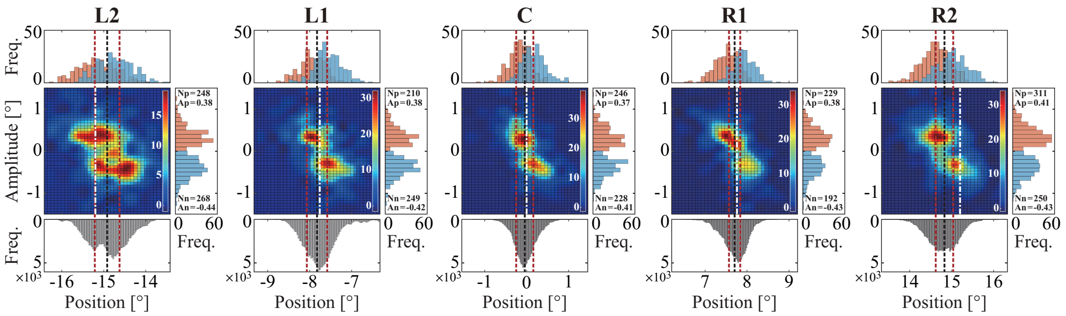

Figure 2.2.3: Relationships between the onset position of MS and its amplitude for each of the five target positions. Color map: two-dimensional histograms of the onset position and amplitude of MS with 0.25° and 0.20° bin widths, respectively, representing the joint frequency of onset positions and amplitudes of MS events. Upper histograms: one-dimensional histograms with a bin width of 0.10° for each of the rightward (red) and leftward (blue) MS events. Right-side histograms: one-dimensional histograms with a bin width of 0.10° for each of the rightward (red) and leftward (blue) MS events. In the right-side histograms, N_p and N_n are the rightward and leftward MS counts, respectively. Similarly, A_p and A_n are the mean amplitude of rightward and leftward MS. For each target condition, the black dotted line represents the mean value of the GZ time series, and the red dotted lines on both sides of the black line represent ±SD away from the mean value of the GZ time series. The dashed white line represents the fixation target position in each target condition.

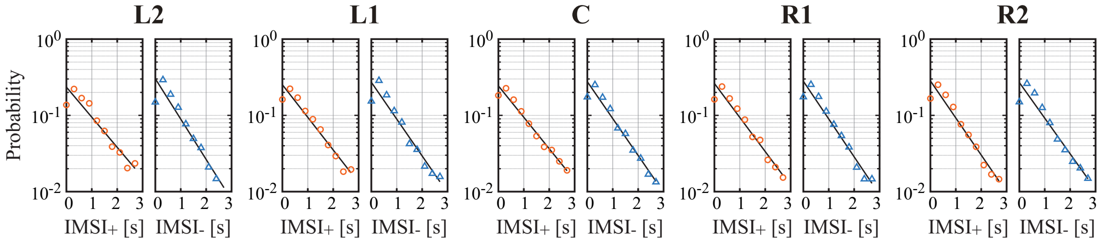

Figure 2.2.4: Semi-log plot of the probability of inter-microsaccadic intervals (IMSI) of all left/right MS across all subjects, with a regression line (black line) in each condition. IMSI_+plotted by the orange circles are the IMSI of rightward MS, and IMSI_- plotted by the blue triangles are the IMSI of leftward MS.

all sampling path from all subjects (Figure 2.2.6, in which the plotted points represent single sampling paths across all subjects). Negative correlations between them were apparent for all target positions. In addition, they were distributed along the line given by Equation (2.1.8) that is satisfied when the centripetal DRT and centrifugal

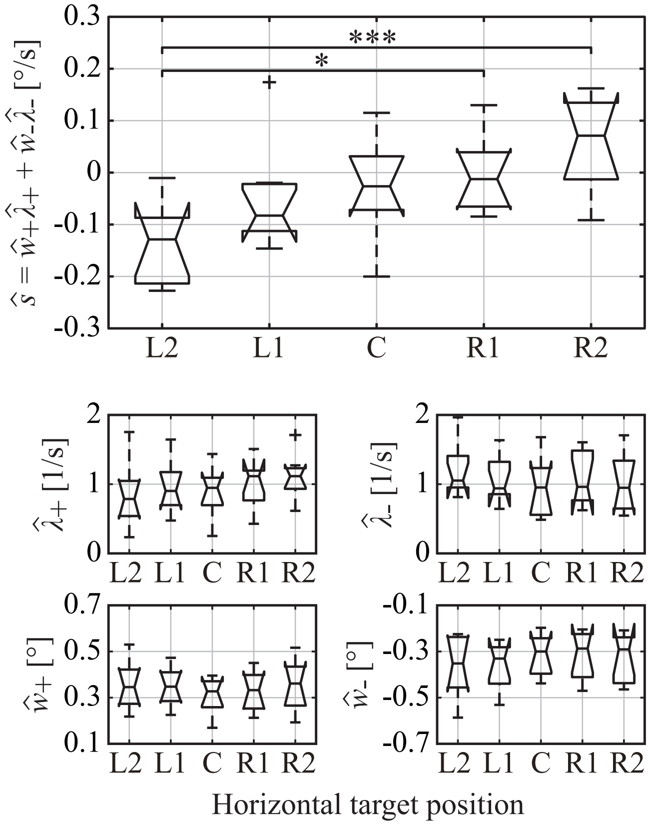

Figure 2.2.5: Boxplots of the estimated amplitude and occurrence frequency of right/left MS, and the total trend generated by total MS across all subjects. $\hat{w}_+$, $\hat{w}_-$, $\hat{\lambda}_+$, and $\hat{\lambda}_-$ represent the subject-wise mean values of the right/left MS amplitude and occurrence frequency, respectively. $\hat{s} \triangleq \hat{w}_+\hat{\lambda}_+ + \hat{w}_-\hat{\lambda}_-$ is the estimated total trend of MS reconstructed from $\hat{w}_+$, $\hat{w}_-$, $\hat{\lambda}_+$, and $\hat{\lambda}_-$. Single and triple asterisks indicate a significant difference between the groups at the 5 and 0.1% significance level, respectively.

MS are completely counterbalanced.

The vertical green line and the horizontal red line in each panel of Figure 2.2.6 represent the mean values μ_{DRT} and s across all subjects. The green line μ_{DRT} shifted more to the right (positive direction) as the target was displayed more to the left (negative direction), and they shifted more to the left (negative direction) as the target was displayed more to the right (positive direction), which was consistent with the lower middle panel of Figure 2.2.1. The red line s shifted more downward (negative direction) as the target was displayed more to the left (negative direction), and they shifted more upward (positive direction) as the target was displayed more to the right (positive direction), which was consistent with Figure 2.2.1, lower right panel and Figure 2.2.5, upper panel.

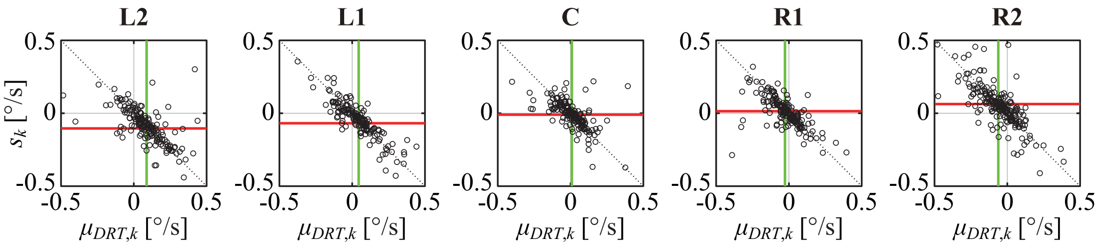

Figure 2.2.6: Scatter plot of a DRT trend $\mu_{\mathrm{DRT},k}$ and the reconstructed MS trend s_k for the kth sample paths across all samples of all subjects for each target position. The green vertical line and the red horizontal line represent the mean value of $\mu_{\mathrm{DRT},k}$ and s_k, respectively. The dotted black line is the complete balanced condition defined by Equation (2.1.8).

2.3 Discussion

2.3.1 Summary

The GZ time series was decomposed into DRT and MS time series. The DRT and MS time series showed unidirectional linear trends in opposite directions. The slope (i.e., the velocity) of the linear trends altered depending on the horizontal position of the fixation target. DRT during inter-MS intervals tended to migrate toward the front-facing position, and MS pulled back the GZ position toward the fixation target intermittently. MSD analysis of the GZ and DRT time series clarified that the GZ time series (FEyeM) behaved like Brownian motion on the short-time scale (0.002 - 0.1 s) and exhibited antipersistence on the long-time scale (0.2 - 10 s), whereas the DRT time series was similar to the Brownian motion over the entire time scale (0.2 - 10 s). These diffusion characteristics were common for all conditions at the fixation target position, which means that the stochastic property of diffusion in DRT alone, such as positive persistence, might not be the major determinant of the unidirectional linear trend of DRT. In other words, the GZ relaxes very slowly (0.1°/s) with the centripetal DRT toward the front-facing position during inter-MS intervals caused by a deterministic driving force, as if there always exists a quasi-stable equilibrium posture in the front-facing position.

2.3.2 Comparison of the Centripetal DRT Trend With Previous Studies

The linear trend (velocity) of the centripetal DRT was at most about 0.1 °/s at the L2 and R2 conditions placed at 15.2 ° leftward and rightward shifted positions, respectively (Figure 2.2.1). Centripetal DRT velocity estimated by Bertolini et al. (2013) was about 0.3 °/s at the corresponding eccentricity, i.e., for the L2 and R2 conditions, which was three times larger than the velocity estimated by the current study. One of the possible causes of this discrepancy is that Bertolini et al. measured DRT velocity in the transient state, that is, not during persistent GZ fixation but during GZ tracking of a quasi-fixation LED target that flashed briefly for 0.05 s every 2 s and shifted between -40° and 40° synchronously with the flash. Such an experimental setting might affect DRT velocity because the GZ in this case might not be able to settle to its steady state within the short time of 0.05 s.

2.3.3 Random-Walk Analysis

The unit slope of the centripetal DRT time series in the Brownian motion analysis (diffusion plot) suggests that the linear trend of the centripetal DRT is not caused by positive persistence of the DRT time series for the following reason, which can be clarified as follows. First, let us consider a random process with positive persistence, i.e., an increment of the process is followed by an increment in the same direction as the previous increment with probability greater than 1/2. Due to this property of positive persistence, the process with positive persistence tends to exhibit a drift-like behavior in one direction. Note that a process with positive persistence exhibits a Hurst exponent $H > 1/2$ and the scaling exponent (a slope of the diffusion plot) $2H > 1$. On the other hand, Brownian motion is neutral in terms of persistence. Namely, an increment of the Brownian motion is independent of the successive increment, and its scaling exponent (a slope of the diffusion plot) is 1, as in the DRT time series. Based on this consideration, we can conclude that the linear trend in the centripetal DRT is not caused by positive persistence of the DRT time series. This result suggests that the linear trend in the DRT time series is caused by a deterministic drifting component. Indeed, if we consider a random process $X(t) \equiv t + B(t)$, where t is a linear trend proportional to time and $B(t)$ is the Brownian motion, it can be confirmed that X(t) exhibits a linear trend and the scaling exponent (the slope of the diffusion plot) is 1.

The diffusion property of the GZ time series characterized by the MSD analysis showed a crossover phenomenon at the critical time lag around 0.1 - 0.2 s that separates the Brownian-motion-like behavior in the short-time scale and antipersistence on the long-time scale, regardless of the horizontal eccentricities (Figure 2.2.2). As the mean MS frequency was about 2 Hz, the Brownian-motion-like behavior of the GZ time series on the short-time scale must be dominated by that of the DRT time series. Indeed, the MSD of the GZ time series was similar to that of the DRT time series on the short-time period (0.002 - 0.1 s). As the scaling exponent (2H) of the DRT time series was close to 1 for both short- and long-time scales, we could conclude that the diffusion property of DRT can be modeled by the Brownian motion over the entire time period (0.002 -

10 s). On the other hand, the antipersistence with the scaling exponent less than 1 of the GZ time series on the long-time scale (0.2 - 10 s) might be caused by MS that counteracted the diffusion of DRT.

The result of random-walk analysis was qualitatively consistent with the pioneering research by Engbert and Kliegl (2004), but quantitatively different. In their study, the critical point of FEyeM appeared around 0.02 - 0.04 s, whereas the critical point of this study was located at around 0.1 - 0.2 s in this study, i.e., about five times larger for the current study. Possible reasons for the difference could be the dimension and length of FEyeM of interest. They applied the random-walk analysis to a two-dimensional FEyeM measured for 3 s, whereas we used a one-dimensional (horizontal) FEyeM recorded up to 30 s with a typical length of $T_{\mathrm{GZ}} \sim 16$ s for the GZ time series. Thus, direct comparisons between the results and their study are less meaningful. However, the diffusion properties of FEyeM may change according to the spatial and temporal size of interest. Nevertheless, as discussed above, because the critical time lag (crossover point) of the MSD analysis of FEyeM must be closely related to the occurrence timing and amplitude of MS, the crossover point of the estimate might be more plausible from a mechanistic viewpoint.

2.3.4 FEyeM as GEN With More Randomness and Slower Centripetal DRT Trend Compared to EPN

This study revealed that alternating repetitions between centripetal drifts and centrifugal saccades as in physiological GEN, also referred to as EPN during FEyeM with large horizontal eccentricities, even during FEyeM with small horizontal eccentricities, but with slower centripetal DRT and more stochasticity in the oscillation period. GEN stochasticity during FEyeM can be characterized by the SD of the inter-(micro)saccadic intervals. In this study, both the mean and SD of the leftward and the rightward IMSI were the inverse of the MS rate for the Poisson-point-process, which were about 1.25 s. In addition to this randomness, the major cause of GEN stochasticity during FEyeM was that MS occurred not only in the centrifugal direction against centripetal DRT, but also in the centripetal direction, which lowered the periodicity of GEN during FEyeM. On the other hand, EPN is much more periodic because MS-like jumps apparently occurred only in the centrifugal direction in EPN (Abel et al., 1978; Shallo-Hoffmann et al., 1990) although the SD of the oscillation period for EPN (Shallo-Hoffmann et al., 1990) is not much different from the SD of the IMSI during FEyeM. In this way, the stochasticity of the GEN-like behavior during FEyeM was much larger than EPN with large eccentricities. This finding is novel, which might contribute to a deeper understanding of both physiological GEN and FEyeM. The stochasticity of GEN can be argued as follows. In front-looking, MS drivers are influenced by a variety of factors, such as proper foveating, and peripheral attention. On the other hand, when looking far to the side, all of these factors are trumped by a bigger force favoring to relax the eye muscles back to the primary position (resulting in the centripetal drift followed by corrective centrifugal saccades). In other words, the properties of FEyeM may not be fully stochastic and are influenced by a variety of task demands; a demand of eccentric GZ fixation might add an extra factor of the eye relaxing back to its primary position, which might appear it somehow “reduces” stochasticity.

The time constant of the exponential centripetal DRT can be defined as the quotient of the difference between the target position and the equilibrium position divided by a DRT trend, which characterizes the leakiness of the oculomotor velocity-to-position neural integrator (Kheradmand and Zee, 2011). If the equilibrium point is assumed to be at the horizontal center of 0° , the time constant obtained from this study was very slow, which was about 250 s if calculated from the mean DRT trend, and about 85 s even in the smallest case. These time constants are much larger than the time constant of a DRT trend in the periodic EPN, and also larger than the time constant of the centripetal drifts in the previous studies (Becker and Klein, 1973; Robinson et al., 1984; Eizenman et al., 1990; Reschke et al., 2006). Particularly, in previous studies, subjects were required to memorize and fixate continuously on the position of the fixation target presented instantaneously in complete darkness, but in the present study, fixation target position was presented continuously in the presence of display light. To the best of my knowledge, this is the first study to show the existence of the slow centripetal DRT in FEyeM at small target angles other than in complete darkness with large eccentricities.

2.3.5 Possible Mechanisms of the Centrifugal MS Trend Generation

Linear regression analysis of the MS time series revealed that the centrifugal MS trend counterbalanced the centripetal DRT trend (Figure 2.2.1), and the MS trend was generated by the target position-dependent small modulation of the total MS amplitudes (Table 2.2.1) as well as the target position- and jump direction-dependent small modulation in the occurrence frequency of MS events (Figure 2.2.5), albeit without statistical significance in these modulations. Despite the absence of significant position-dependent differences in each of the rightward and leftward MS amplitudes, a significant dependence of the target position on the mean total MS amplitude, which averages the MS amplitudes without distinction between rightward and leftward jumps, implies a non-negligible dependence of the target position on MS amplitude for each of the rightward and leftward MS. A detailed analysis of the MS time series and their centrifugal trend was performed based on the four parameters of MS, i.e., $\hat{\lambda}_+$,$\hat{\lambda}_-$,$\hat{w}_+$, and $\hat{w}_-$, which represent the subject-wise means of rates and amplitudes of the rightward and the leftward MS events, together with the combination of those as $\hat{s}$, which is the slope of the centrifugal trend of MS (Figure 2.2.5). Such an analysis revealed the complex mechanism of how the centrifugal MS trend is generated. None of the four parameters did not show significant dependence on the target positions, while ŝ reconstructed from the four parameters explained the dependence of the target position on the velocity of the centrifugal trend (Figure 2.2.5, top panel). This result implies that MS amplitude and frequency were co-modulated (though very slightly for each of them own) to generate the target position-dependent slope of the centrifugal trend of MS, which counterbalanced the centripetal DRT trend. It has been known that the occurrence frequency of MS is suppressed when subjects concentrate on the fixation intentionally (Winterson and Collewun, 1976; Bridgeman and Palca, 1980). A typical example of such an amplitude modulation occurs when subjects are asked to perform a macroscopic voluntary saccade to track a sudden change in the target position. In this case, the MS amplitude during GZ fixation becomes small prior to the onset of the voluntary saccade, suggesting that MS and voluntary saccades may share a common neural control mechanism. Recent studies have begun to elucidate a detailed MS generation and modulation mechanism by a cortical neural network (e.g., frontal eye field and primary visual cortex) and a subcortical neural network (e.g., superior colliculus and cerebellum), which adapt MS dynamics to a varied situation (Hafed et al., 2009, 2021; Hafed, 2011; Otero-Millan et al., 2011; Arnstein et al., 2015; Peel et al., 2016; Willeke et al., 2019; Buonocore et al., 2021). Such functional neuroanatomy could provide a mechanistic basis of the cooperative control and/or co-modulation of MS amplitude and frequency that were characterized in this study. Establishing a computational model for this mechanism is the next study.

2.3.6 Target Position-Dependent Counterbalance Between the Linear Trends of DRT and MS

The scatter plot between the linear trends of DRT characterized by $\mu_{\mathrm{DRT},k}$ and MS characterized by s_k showed that centripetal DRT and centrifugal MS satisfied Equation (2.1.8, and the counterbalance point between them (i.e., the point at which the mean linear trends of DRT and MS coincided in the $\mu_{\mathrm{DRT},k}$-s_k plane) in Figure 2.2.6 was shifted from the origin along the line $\mu_{\mathrm{DRT}} = -s$ of Equation 2.1.8), depending on the target position. This target position-dependent shift of the counterbalance point along the line of Equation 2.1.8) explains the GZ control mechanism during GZ fixation with eccentricities because the GZ fixation might lose its stability if the counterbalance point between DRT and MS was shifted away from the line of Equation 2.1.8). Interestingly, it seems that eye blinks might reset the GZ position to the desired target position when the counterbalance between DRT and MS was shifted away from the line of Equation 2.1.8) based on a visual inspection of the upper middle and right panels of Figure 2.2.1, where the DRT and/or the MS series tended to be terminated by eye blink, making the length of those sample paths shorter than the others.

2.3.7 Oculomotor Control Perspective

Fixation on a target shifted to the left or right from the center position is an attention-demanding motor task. Therefore, it is expected that the motor center and motor neurons need to maintain the tonic balance of the tension between the medial and lateral rectus muscles of each eyeball. The existence of migration trends in DRT implies that the tonic control of these antagonist muscles is lost intermittently, and the GZ diffuses away from the fixation target position during “resting” intervals. Furthermore, in this situation, it is conceivable that a stable eyeball posture appears transiently somewhere in the front-facing-side, toward which the eyeball posture may be relaxed, leading to the generation of centripetal DRT. From the viewpoint of motor control, when one fixates on a target position deviated from the center to the left or right, his/her eyeballs are always drawn to their most stable postures by the DRT, which is internal noise, and the errors that increase continuously during the DRT interval are intermittently and stochastically reduced by MS reflecting the control input for correction. This is consistent with existing research with respect to the role of MS in improving fixation stability (Cornsweet, 1956; Engbert and Kliegl, 2004; Ko et al., 2010).

The intermittent loss of tonic balance between antagonist muscles could be due to neuronal fatigue or more strategic optimization, such as to minimize energy expenditure or to increase flexibility in preparation for oculomotor demands.

Chapter 3

Neuromechanical Modeling for Stochastic Gaze-evoked Nystagmus

In this chapter, the neuromechanical model of stochastic GEN was constructed to understand better the detailed neural control mechanisms of DRT and MS, aiming for an integrated understanding of FEyeM and GEN. Understanding the mechanisms enable us to generate the very slow DRT with a maximum velocity of about 0.1 °/s is not easy. The mechanical time constant of the oculomotor system calculated by the mechanical parameters estimated from human extraocular muslces was up to 1.58 s (Childress and Jones, 1967; Robinson et al., 1969), which is not enough large to reproduce the slowness of the centripetal DRT characterized in the Chapter 2. The main purpose of this model study is to propose a way of neural control that can reproduce the slowness of centripetal DRT.

3.1 Background

3.1.1 Estimation of the Time Constant of Centripetal DRT

This section explains the background of the slowness of centripetal DRT, which can be characterized by the time constant.

Assuming that the DRT is approximated by an exponential relaxation curve with time constant τ moving from the initial position $\theta(0)$ to the equilibrium position $\bar{\theta}$, the gaze position $\theta(t)$ during centripetal DRT can be expressed as

$$\theta(t) = \bar{\theta} + (\theta(0) - \bar{\theta})e^{-\frac{t}{\tau}}. \tag{3.1.1}$$

Taylor expansion of this equation yields the following equation.

$$\theta(t) = \theta(0) + \left.\frac{d\theta(t)}{dt}\right|_{t=0} + \left.\frac{d^2\theta(t)}{dt^2}\right|_{t=0} + ... \tag{3.1.2}$$

Ignoring second and higher order terms, the linear function is approximately obtained:

$$\theta(t) \approx \theta(0) - \frac{\theta(0) - \bar{\theta}}{\tau}t. \tag{3.1.3}$$

Since the coefficient of t is corresponding to the slope of the DRT time series μ_{DRT}, the following relationship holds:

$$\mu_{\text{DRT}} = -\frac{\theta(0) - \bar{\theta}}{\tau}. \tag{3.1.4}$$

Rewriting this equation, for a given μ_{DRT}, time constant τ can be calculated as,

$$\tau = -\frac{\theta(0) - \bar{\theta}}{\mu_{\text{DRT}}}. \tag{3.1.5}$$

The equilibrium position $\bar{\theta}$ during (eccentric) fixation is unknown. Assuming that the equilibrium position is located at the center position (i.e. $\bar{\theta} = 0$), Equation 3.1.5 becomes simpler as,

$$\tau = -\frac{\theta(0)}{\mu_{\text{DRT}}}. \tag{3.1.6}$$

Since the estimated value of μ_{DRT} was up to about 0.1 °/s when the fixation target located at -15.2 °. In this situation, if the fixation started at the target position (i.e. $\theta(0) = -15.2$), then Equation 3.1.6 let us calculate the time constant τ as 152 s. In fact, estimation of the time constant of centripetal DRT based on the above calculations yielded the average value of 253 s across all subject for the most eccentric fixation condition, which is slower than the known time constant of GEN of 10-70 s (Becker and Klein, 1973; Robinson et al., 1984; Eizenman et al., 1990; Reschke et al., 2006). The time constant larger than 100 s is extremely slow as a time constant for biological systems. In the following sections, we consider how such very slow time constant of centripetal DRT can be generated.

3.2 Methods

The neuromechanical model was constructed to study the mechanisms generating and controlling centripetal DRT (Drifts-tremor) and centrifugal MS (microsaccades) at small horizontal eccentricities. A rigid eyeball, Hill-type muscles and its neural activities, non-muscular tissues, and noise terms constitute the neuromechanical model. The Hill-type muscle models of horizontal extraocular muscles (the medial and lateral rectus muscles) drive the horizontal rotation of the rigid eyeball against the viscoelasticity of the non-muscular tissues with noise. The rigid-body rotational motion of the eyeball was obtained as the numerical solution of the equation of motion with the muscle contraction force, passive viscoelastisity, and noise. In other words, the neuromechanical model takes in the form of a stochastic differential equation.

3.2.1 Stochastic Equation of Motion of Horizontal Eye Rotation

A force balance between antagonist muscles, i.e., the lateral rectus (LR) and the medial rectus (MR), determines the abduction/adduction rotation of the eyeball (the rotation angle θ) and the horizontal position of gaze, where LR and MR are responsible for abduction and adduction of the eyeball, respectively. For simplicity, only a single eyeball at the right is considered in this section, and it was assumed that the muscles of LR and MR have exactly the same natural length $\ell_{i,res}$ and the same properties for passive and active contractile elements. A muscular force $F_i\left(\alpha_i, \ell_i(\theta), \dot{\ell}(\dot{\theta})\right)$ is a function of the neural activation level $\alpha_i \in [0,1]$, muscle length $\ell_i(\theta)$, and muscle-length contractile velocity $\dot{\ell}_i(\dot{\theta})$ of either LR muscle ($i = 1$) or MR muscle ($i = 2$). That is, the muscle forces of LR and MR are represented by $F(\alpha_1, \ell_1(\theta), \dot{\ell}_1(\dot{\theta}))$ and $F(\alpha_2, \ell_2(\theta), \dot{\ell}_2(\dot{\theta}))$, respectively. A dot and two dots above a symbol are used to indicate first and second order derivative taken with respect to time (e.g. $\dot{x} \equiv \frac{dx}{dt}, \ddot{x} \equiv \frac{d^2x}{dt^2}$). Then, the equation of motion for the horizontal rotation of the eyeball can be expressed as

$$I\ddot{\theta} = (F_1(\alpha_1, \ell_1(\theta), \dot{\ell}_1(\dot{\theta})) - F_2(\alpha_2, \ell_2(\theta), \dot{\ell}_2(\dot{\theta})))r - B_p\dot{\theta} + \sigma_T\xi_T \tag{3.2.1}$$

where I is the moment of inertia of the eyeball, and r is the moment arm of the muscle. F_1, F_2 is the contraction force of horizontal extraocular muscles (the medial and lateral rectus muscles), B_p is a linear damping coefficient,representing friction forces due to non-muscularcauses. σ_T is noise intensity. The additive noise $\sigma_T\xi_T$ is white Gaussian noise (WGN) with noise intensity σ. Note that ℓ_i and $\dot{\ell}_i$ ($i = 1, 2$) are determined as functions of θ and $\dot{\theta}$, respectively.

The rotation angle θ is zero [°] when the eyeball faces the front, and the clockwise direction is positive. The force of the horizontal extraocular muscles was modeled by the Voigt model that consists of active contractile element (CE) and parallelly connected passive elastic element (PE) of muscle and tendon except for series elastic element as shown in Figure 3.1.1. Since the Voigt model that lacks series elasticity was sufficient to represent active control of damping through co-contraction of antagonistic muscles in a three-link biomechanical limb (Heitmann et al., 2012), the model was modified and applied to the oculomotor system.

The contraction force of horizontal extraocular muscles, F_i ($i = 1, 2$), can be described as the function of the neural activity α_i and muscle length $\ell_i(\theta)$ and its velocity $\dot{\ell}_i(\theta)$:

$$F_i\left(\alpha_i, \ell_i(\theta), \dot{\ell}_i(\theta)\right) = \alpha_i F_{\max} f_\theta(\ell_i(\theta)) f_\omega\left(\dot{\ell}_i(\dot{\theta})\right) + k_{\mathrm{pe}}(\ell_i(\theta) - \ell_{i,\mathrm{res}}) \quad (i = 1, 2) \tag{3.2.2}$$

where α_i is the coefficient of the each muscle neural activity taking between 0 to 1 ($0 < \alpha_i < 1$), $F_{\max}$ is the maximum contraction force of the muscle, $f_\theta(\ell_i(\theta))$ is the force-length relationship, $f_\omega(\dot{\ell}_i(\dot{\theta}))$ is the force-velocity relationship, k_{pe} is the passive elastic coefficient, and $\ell_{i,res}$ is the natural length of each muscle. To be exact, the maximum contraction force $F_{\max}$ is different between the medial rectus and the lateral rectus as $F_{\max,i}$ ($i = 1, 2$). In this study, bilateral symmetry of the mechanical properties of the oculomotor system was supposed for simplicity. That is the reason the constant maximum contraction force $F_{\max}$ was used not as $F_{\max,i}$. Figure. 3.2.1 shows schematic views of the model.

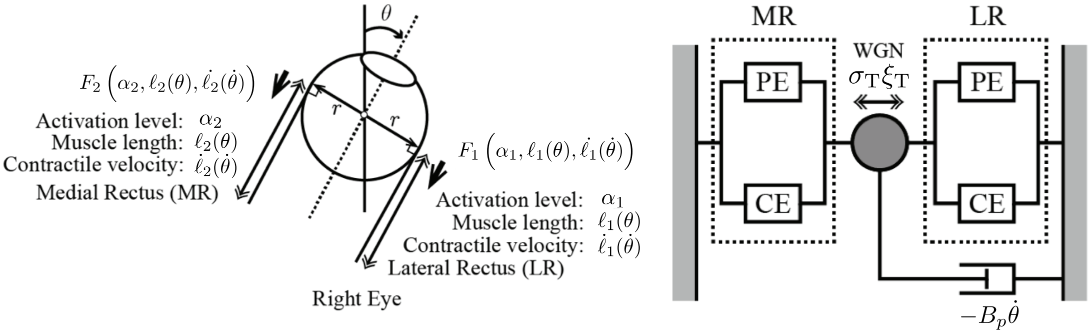

Figure 3.2.1: Schematic views of the model.

The force-length relationship $f_\theta(l_i(\theta))$ and the force-velocity relationship $f_\omega(\dot{l}_i(\dot{\theta}))$ are complex non-linear function in real. To make an alanysis easy, $f_\theta(l_i(\theta))$ and $f_\omega(\dot{l}_i(\dot{\theta}))$ were linearized around the origin:

$$f_\theta(\ell_i(\theta)) = a_\theta\theta + b_\theta, \tag{3.2.3}$$

$$f_\omega(\dot{\ell}_i(\dot{\theta})) = a_\omega\dot{\theta} + b_\omega, \tag{3.2.4}$$

where a_θ is the slope of linearized $f_\theta(\ell_i(\theta))$, b_θ is the intercept of linearized $f_\theta(\ell_i(\theta))$, a_ω is the slope of linearized $f_\omega(\dot{\ell}_i(\dot{\theta}))$, and b_ω is the intercept of linearized $f_\omega(\dot{\ell}_i(\dot{\theta}))$.

All mechanical parameters are listed in the table 3.2.1.

Table 3.2.1: Mechanical and neural parameters

Parameter	Units	Definition	Value	Reference
m	kg	Mass of the eyeball	7.5×10^{-3}	Gunawardane, 2019
r	m	Radius of the eyeball	1.2×10^{-2}	Bekerman, 2014
I	$\mathrm{kg} \cdot \mathrm{m}^2$	Moment of inertia of the eyeball	4.3×10^{-7}	By calculation
F_{max}	N	Maximum force of CE	9.0×10^{-1}	Robinson, 1969
K_p	$\mathrm{N} \cdot \mathrm{m}/^\circ$	Elastic coefficients of PE	2.3×10^{-5}	Robinson, 1969
B_p	$\mathrm{N} \cdot \mathrm{m} \cdot \mathrm{s}/^\circ$	Damping coefficient of non-muscular tissue	7.2×10^{-5}	Childress, 1967
a_θ	$1/^\circ$	Slope of f_θ linearized around the origin	1.3×10^{-2}	Robinson, 1969
b_θ	–	Intercept of f_θ linearized around the origin	5.2×10^{-1}	Robinson, 1969
a_ω	$\mathrm{s}/^\circ$	Slope of f_ω linearized around the origin	2.4×10^{-3}	Priamikov, 2016
b_ω	–	ntercept of f_ω linearized around the origin	1.0	Priamikov, 2016

3.2.1.1 Model of the Neural Activation

The muscle neural activity $\alpha_i(t)$ that can generate impulsive contraction force was modeled as

$$\begin{aligned} &\frac{d\alpha_i(t)}{dt} = -\frac{\alpha_i(t) - \alpha_{i,\text{laz}}}{\tau_{\alpha_i}} + A_i \sum_j \delta(t - t_j) + \sigma_{\alpha_i}\xi_{\alpha_i}, \\ &(t = t_j \text{ when } \theta(t) < \theta_{th,-}, \theta_{th,+} < \theta(t)), i = \{1, 2\}, \end{aligned} \tag{3.2.5}$$

where $\alpha_{i,laz}$ is a supposed lazy target value of the neural activity, τ_{α_i} is a time constant of decay, A_i is a neural jump width for generaing impulsive contraction force, $\delta(t)$ is delta function, and $\sigma_{\alpha_i}\xi_{\alpha_i}$ is an additive neural noise term of the standard WGN ξ_{α_i} with noise intensity σ_{α_i}.

3.2.1.2 Equlibrium Position

For a given $\alpha_1(t)$ and $\alpha_2(t)$, finding $\theta(t)$ for which the sum of the torques becomes 0, the equilibrium gaze position at time t, $\bar{\theta}(\alpha_1(t), \alpha_2(t))$ is derived as,

$$\bar{\theta}(\alpha_1(t), \alpha_2(t)) = \frac{rF_{max}(\alpha_1(t) - \alpha_2(t))b_\theta b_\omega}{rF_{max}(\alpha_1(t) + \alpha_2(t)a_\theta b_\omega + 2K_p)}. \tag{3.2.6}$$

3.2.1.3 Numerical Analysis

Most of stochastic differential equations are difficult to be solved analytically. Numerical solution of the stochastic equation of motion (Eq.3.2.1) was obtained by Euler method with small time step less than 10^{-5}.

3.2.1.4 Simulated GZ, DRT, and MS Time Series

Numerical solution of the stochastic equation of motion of horizontal eye rotation $\theta(t)$ is the time series corresponding to the gaze (GZ) time series, $X_{\text{GZ}}(t)$, because they include both drifts-tremor (DRT) and microsaccades (MS). Then, I rewrite $\theta(t)$ as $X_{\text{GZ}}(t)$

$$X_{\text{GZ}}(t) \equiv \theta(t) \tag{3.2.7}$$

As described in Chapter 2, for a given $X_{\text{GZ}}(t)$, DRT and MS time series can be defined because we knows what components are microsaccades.

3.2.2 Random Walk Analysis of Simulated GZ and DRT Time Series

Diffusion properties of $X_{\text{DRT}}(t)$ and $X_{\text{GZ}}(t)$ were characterized by the mean square displacements (MSD) and calcualted as functions of the time lag $\tau \cdot \delta_s$ defined as follows:

$$\langle (\Delta x_{\text{GZ}}(\tau))^2 \rangle = \frac{1}{N - \tau} \sum_{j=1}^{N-\tau} |x_{\text{GZ}}(j + \tau) - x_{\text{GZ}}(j)|^2, \tag{3.2.8}$$

$$\langle (\Delta x_{\mathrm{DRT}}(\tau))^2 \rangle = \frac{1}{N-\tau} \sum_{j=1}^{N-\tau} \left| x_{\mathrm{DRT}}(j+\tau) - x_{\mathrm{DRT}}(j) \right|^2, \tag{3.2.9}$$

where N is the total data number included in the time interval of T_{GZ} for a given sample path. Note that MSD is also known as the stabilogram diffusion analysis (Collins and De Luca, 1993; Engbert and Kliegl, 2004). Double-log plots of MSD as a function of τ for each target position were obtained by performing ensemble average over all sample paths for each subject. From the estimated MSD scaling exponent, the degree of diffusion of $X_{\mathrm{DRT}}(t)$ and $X_{\mathrm{GZ}}(t)$ was characterized in comparison with the Brownian motion that exhibits the unity scaling exponent (which is equal to $2H$ for the Hurst exponent H) with its variance determined as the averaged variance of the increment per second of the DRT time series. For comparison to the experimental result, simulated GZ and DRT time series were down-sampled to 500 Hz, which is the sampling frequency of the human gaze measurement. Ensemble average of MSD of 20 sample paths for each target was calculated to draw the figure showed in Result.

3.2.3 Temporal Structure of Simulated MS Time Series

Temporal structure of MS time series was characterized by the histogram of inter-microsaccadic intervals (IMSI) in the right and left directions. Since probability of the occurrence of MS events has been approximated by a Poisson point process (Engbert, 2006), for which the IMSI obeys the exponential distribution with the exponential probability density function (PDF), the histograms of IMSI in each of the rightward (+) and leftward (−) directions were approximated by

$$p(x; \lambda_{\pm}) = \lambda_{\pm} e^{-\lambda_{\pm} x} \tag{3.2.10}$$

for the IMSI values $x = \mathrm{IMSI}_{+}$ between subsequent rightward MS events with the occurrence frequency λ_{+} and for $x = \mathrm{IMSI}_{-}$ between subsequent leftward MS events with the occurrence frequency λ_{-}.

3.3 Results

3.3.1 Simulated GZ, DRT, and MS Time Series

The results of neumerical simulation for the equilibrium position of 15° and −15° are shown in Figure 3.3.1, 3.3.2. The centripetal DRT was generated as eye movements relaxing toward the lazy equilibrium position that existed slightly medial to the target position. The position of the equilibrium point changed rapidly due to the impulse-like neural activity generated when the gaze position crossed the threshold. The centrifugal MS were generated by the rapid gaze transition following the rapid change of the equilibrium position toward the outside. Figure 3.3.3 shows that the model have an ability to reproduce centripetal DRT and centrifugal MS that have a same velocity properties quantified in the experimental part.

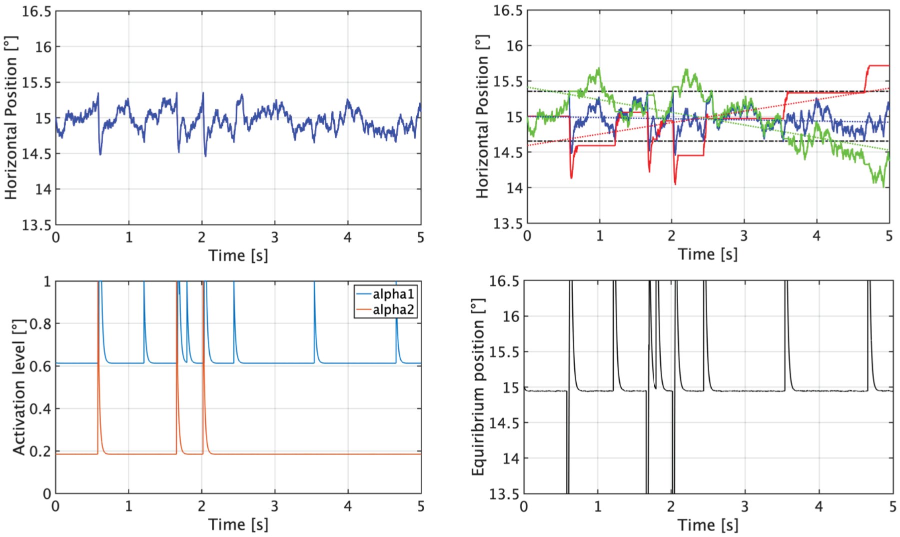

Figure 3.3.1: Simulation for the target position of 15°. Top-left figure shows simulated $\theta(t)$, $X_{\mathrm{GZ}}(t)$, for 5 seconds. Top-right figure shows $X_{\mathrm{GZ}}(t)$ (blue line), $X_{\mathrm{DRT}}(t)$ (green line) and $X_{\mathrm{MS}}(t)$ (red line). Bottom-left figure shows simulated neural activities, $\alpha_1(t)$ and $\alpha_2(t)$, corresponding to the $X_{\mathrm{GZ}}(t)$ shown in top-left and top-right figure. Bottom-right figure shows equilibrium position, $\bar{\theta}(\alpha_1(t), \alpha_2(t))$, corresponding to the $X_{\mathrm{GZ}}(t)$ shown in top-left and top-right figure.

3.3.2 Relationship Between Laziness and Slowness of Centripetal DRT

Figure. 3.3.3 shows the Relationship between the laziness in the model and the slowness of centripetal DRT. The slowness was strongly dependent on the laizness.

3.3.3 Horizontal Target Position Dependency of Simulated GZ, DRT, and MS Time Series

Figure 3.3.4 upper panels shows all simulated sample paths of GZ time series $X_{\mathrm{GZ}}(t)$, DRT time series $X_{\mathrm{DRT}}(t)$, and MS time series $X_{\mathrm{MS}}(t)$. The least square linear regression line was superposed on each of $X_{\mathrm{GZ}}(t)$, $X_{\mathrm{DRT}}(t)$ and $X_{\mathrm{MS}}(t)$ for each of the five fixation targets. Horizontal target position dependency similar to the experimental result (Figure. 2.2.1) was obtained by choosing proper parameters.

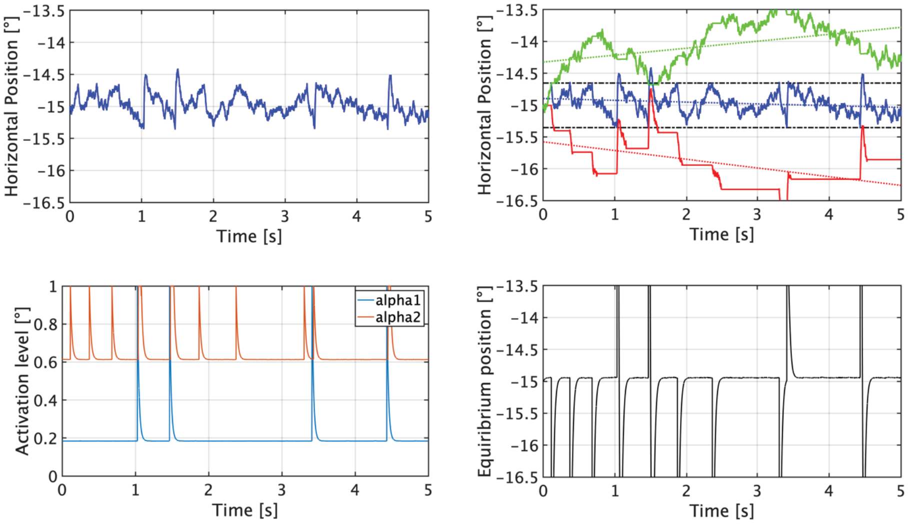

Figure 3.3.2: Simulation for the target position of −15°. Top-left figure shows simulated $\theta(t)$, $X_{\text{GZ}}(t)$, for 5 seconds. Top-right figure shows $X_{\text{GZ}}(t)$ (blue line), $X_{\text{DRT}}(t)$ (green line) and $X_{\text{MS}}(t)$ (red line). Bottom-left figure shows simulated neural activities, α_1 and α_2, corresponding to the $X_{\text{GZ}}(t)$ shown in top-left and top-right figure. Bottom-right figure shows equilibrium position, $\bar{\theta}(\alpha_1(t), \alpha_2(t))$, corresponding to the $X_{\text{GZ}}(t)$ shown in top-left and top-right figure.

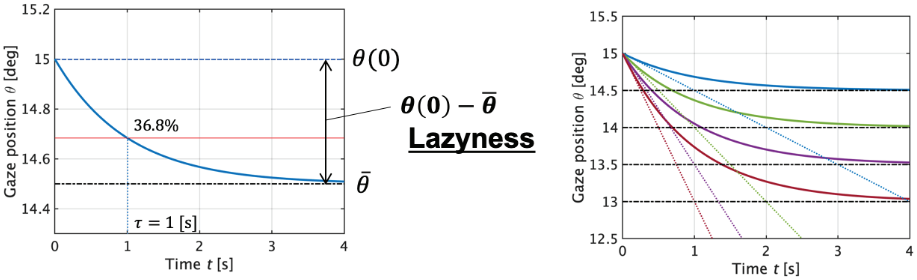

Figure 3.3.3: Relationship between the laziness in the model and the slowness of centripetal DRT

3.3.4 Random-Walk Analysis

Figure 3.3.5 shows the MSD of $X_{\text{GZ}}(t)$ and $X_{\text{DRT}}(t)$ for each of the five target positions. Over a wide range of time lag (0.002 - 10 s), regardless of the horizontal fixation condition, the scaling exponent of the DRT time series, which corresponds to $2H$ for the Hurst exponent H, was about 1, i.e., $H \sim 1/2$. That is, the MSD profile of the DRT time series was similar to the MSD of the Brownian motion, regardless of the target position, despite of the fact that the slope (i.e., the velocity) of the centripetal linear trend of the DRT time series exhibited a clear dependence on the target position.

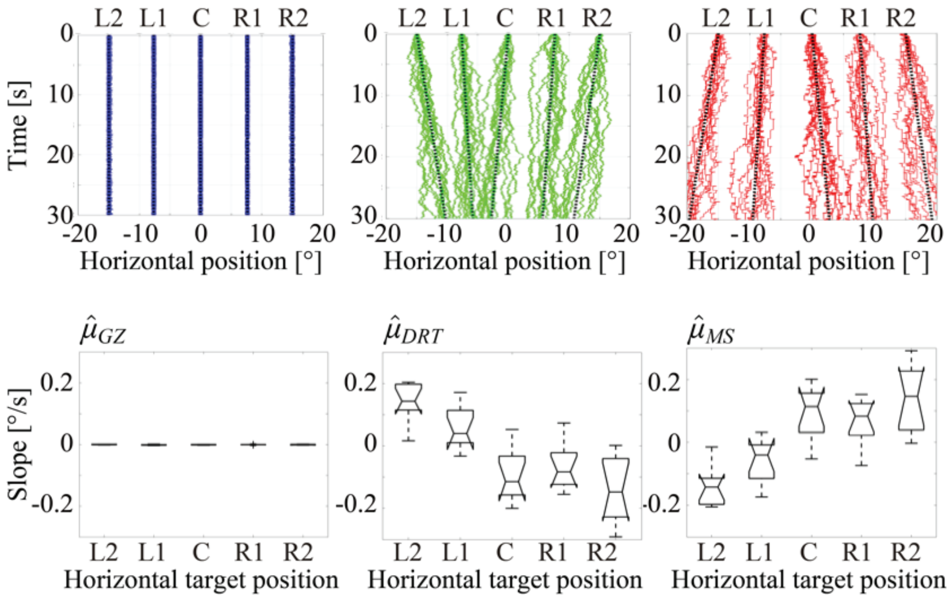

Figure 3.3.4: Horizontal target position dependency of GZ, DRT, and MS time series and the slopes their trend. Upper panels: All sample paths of GZ (left, blue), DRT (middle, green) and MS (right, red) time series from a representative subject were superposed for each of the five target positions. Black dotted lines are the least square linear regression lines, representing the linear trend of the time series for each of the five target positions.

On the other hand, the MSD of the GZ time series $X_{\mathrm{GZ}}(t)$ exhibited a crossover phenomenon, in which the critical point (critical time lag) was located around 0.1 s. The $2H$ scaling exponent of $X_{\mathrm{GZ}}(t)$ for the short-time scale (0.002 - 0.1 s) was about 1, whereas that for the long-time scale (0.1 - 10 s) was almost 0, regardless of the target position. In summary, the MSD of $X_{\mathrm{GZ}}(t)$ and $X_{\mathrm{DRT}}(t)$, i.e., the random-walk property of the GZ and DRT time series did not show the dependence on the target position, despite the fact that the slope (i.e., the velocity) of the centripetal linear trend of the DRT time series and the centrifugal linear trend of the MS time series exhibited a clear dependence on the target position.

3.3.5 Inter-microsaccadic Intervals (IMSI) of Simulated MS

Figure 3.3.6 shows a semi-log plot of the probability of IMSI of all left/rightward MS simulated with a regression line in each condition. The slope of the semi-log plot of the probability, λ_+ and λ_-, was different in target position ranging from about 0.2 to 2.

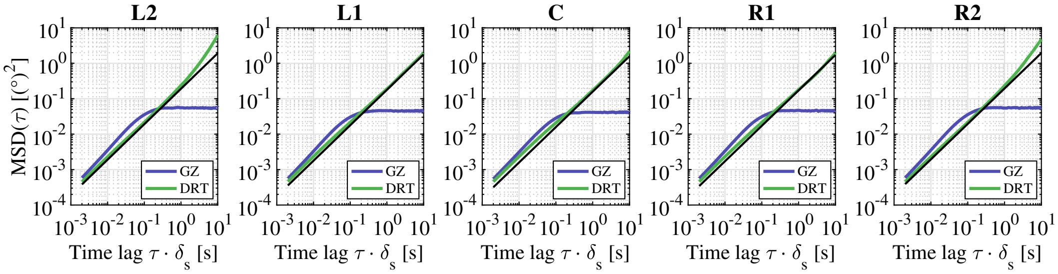

Figure 3.3.5: Mean square displacement (MSD) analysis of the GZ and DRT time series obtained by simulation. The blue and green curves represent, respectively, the MSDs of the GZ and DRT time series. The black lines are the MSD of the Brownian motion for comparison. The MSD curves depicted in each panel are the ensemble average of MSD for each condition.

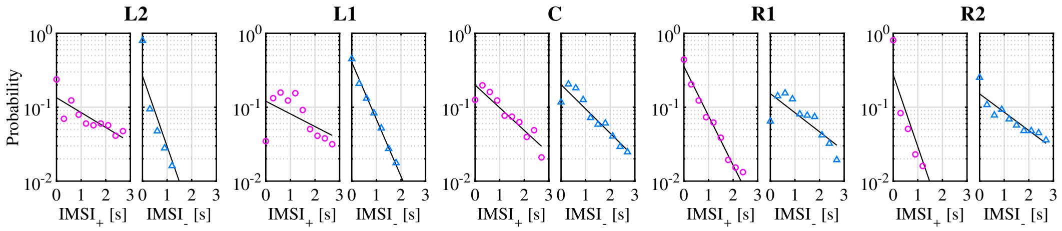

Figure 3.3.6: Semi-log plot of the probability of inter-microsaccadic intervals (IMSI) of all left/rightward MS simulated, with a regression line (black line) in each condition. IMSI_+ plotted by orange circles are the IMSI of rightward MS, and IMSI_- plotted by blue triangles are the IMSI of leftward MS.

3.4 Discussion

3.4.1 Summary

We constructed the neuromechanical model that can reproduce centripetal DRT and centrifugal MS, aiming at an integrated understanding of FEyeM and GEN, which were conventionally considered independent phenomena. The slope of the regression line of the DRT time series reflecting the slowness of centripetal DRT was successfully reproduced as quantitatively to the experimental result. The IMSI that characterizes a temporal structure of MS can also be reproduced in the same order as the experimental result.

3.4.2 Slowness of DRT Time Series

The linear trend of the centripetal DRT was mainly determined by the difference between target position and lazy target position as shown in Figure. 3.3.3. If the target position and lazy target position take the completely same value, the DRT does not generate any linear centripetal trend and MS have never been triggered. The viewpoint suggests that our oculomotor system may unconsciously prioritize not getting tired over the accuracy of the fixation position.

3.4.3 Random-Walk Analysis

Figure 3.3.5 shows that the MSD of the simulated DRT time series was almost the same as the MSD of the Brownian motion for any target position and any time range. This result was consistent with the MSD of the DRT time series experimentally obtained from human subjects (Figure 2.2.2). On the other hand, the MSD of the simulated GZ time series in the long-time scale (0.1 - 10 s) was different from the experimental result (Figure 2.2.2) that exhibited a small scaling exponent of 0.1-0.3. The result that the scaling exponent of the simulated GZ time series in the long-time scale (0.1 - 10 s) was almost 0 means that the GZ time series were completely antipersistent. In other word, GZ time series had a strong negative correlation between its increments in the long-time scale (0.1 - 10 s). The antipersistency of the GZ time series is an obvious outcome because the GZ time series is completely trapped between the inner and outer thresholds and never diffuses across the thresholds. The critical point around 0.1 s and the scaling exponent in the short-time scale (0.002 - 0.1 s) in the MSD of the GZ time series were able to be well reproduced.

3.4.4 Temporal Struction of Simulated MS

IMSI of simulated right/leftward MS have a exponential distribution but the slope of the semi-log plot, λ_+ and λ_+, was different in target position. The amount of λ_+ and λ_+ fall within the range of at most twice and at least 1/2 times the experimentally measured value. In the left/rightward eccentric fixation condition, left/rightward MS occurs more often than right/leftward MS since the slope of the probability distribution in the semi-log plot indicates the mean frequency of occurrence. This is a remarkable indication that this model responds to the change of the centripetal DRT trend according to the gaze eccentricity by modulating the frequency of MS occurrence. Since MS is mainly described by its occurrence frequency and amplitude, improving an amplitude modulation mechanism would make them more similar to human MS. The occurence of MS can be controled by DRT slowness, noise intensity and threshold settings. Each of these factors is intricately interwined. There remains room for further study on how to set the optimal threshold. It is still highly debatable what physical quantity and how much threshold our eye movement system actually generates MS based on. Alternatively, it is possible that MS is simply generated randomly by a stochastic model inside the neural circuitry.

3.4.5 Possibility of Leaky Velocity-to-position Integrator

The most critical consideration to be made going forward is to examine the possibility of the effect of the leaky velocity-to-position integrator. It is known that the gaze position was neurally generated by integrating a neural velocity command in an actual oculomotor system, and the velocity-to-position integrator is leaky (Nakamagoe et al., 2000; Bögli et al., 2021). The amount of leakiness must affect the linear trend of the DRT time series. The neuromechanical model must be modified by adding the equation of the leaky velocity-to-position integrator and examining the mechanisms of how much the leakiness affects the DRT slowness.

Chapter 4

General Discussion and Conclusion

4.1 Summary

The dissertation quantified the characteristics of FEyeM (Fixational Eye Movements) during horizontal less-eccentric fixation and constructed a neuromechanical model that can reproduce such characteristics, aiming at an integrated understanding of FEyeM and GEN (Gaze-Evoked Nystagmus), which were conventionally considered to be independent phenomena. The horizontal position dependency of centripetal DRT (Drifts-Tremor), which characterize stochastic GEN, was experimentally investigated and it is found that their average velocity is about three times slower than the previously known value. Centrifugal MS (Microsaccades) was found to be capable of generating a linear trend counterbalancing the mean velocity of centripetal DRT while being generated in an unmemorized manner. Model analysis reveals that low laziness (i.e., effort to move the equilibrium position closer to the target position) is necessary to reproduce the very slow trend of centripetal DRT. The implementation of the MS frequency modulation mechanism was achieved well. On the other hand, issues remained regarding the amplitude modulation mechanism.

4.2 Role of Laziness in Human Oculomotor System

The primary purpose of the model study in Chapter 3 was to explain how the slowness of centripetal DRT characterized in Chapter 2 was generated, which cannot be described by the mechanical properties of the human oculomotor system. The neuromechanical model study lets us know that the difference between the lazy target position and the actual target position might generate the slowness of the centripetal DRT characterized by the regression line slope of the DRT time series. Laziness and accuracy have a trade-off relationship. Our oculomotor system may unconsciously give up the rigor of the fixation position to conserve energy. The amount of laziness in how precisely we try to fixate on a target differs from person to person, and the difference from person to person may be reflected in the strength of the DRT trend. These individual differences may result from motor learning by the cerebellum resulting from individual environmental differences.

4.3 Diffenrece Between Human Eye Movements and Eye Movements Simulated by the Nuromechanical Model

The crucial difference in human eye movements but not in the eye movements simulated by the neuromechanical model is the presence or absence of eye blinks. The result of the target position-dependent counterbalance between the linear trends of DRT and MS, as shown in Figure 2.2.6, suggests that the eye blinks might reset the gaze position, which makes the length of the inter-blinks intervals distributed and contributes to stable fixation. In other words, centripetal DRT and centrifugal MS are often not perfectly balanced in actual human eye movements. On the other hand, the neuromechanical model that does not have the reset function of blinks must achieve stable fixation with only MS, which must counterbalance the centripetal trend of DRT. This structural difference places stronger constraints on the model's MS. Weakening this constraint so that the MS alone does not have to be perfectly balanced with DRT should make the behavior of the MS more realistic. The difference between the measured human eye movements and simulated eye movements in the random-walk analysis (Figure 2.2.2, 3.3.5) also implies the same interpretation. The model cannot reproduce a weaker negative correlation of the GZ time series between its increments in the long-time scale (0.1-10 s) as human subjects, which exhibits the scaling exponent of 0.1-0.3. The role of the weaker persistency in the GZ time series remains unclear, but a human oculomotor system may provide a more energy-efficient neural control at the expense of gaze-holding stability.

Appendix A

Decomposing GZ Time Series Into DRT and MS Series

First, for a given raw-GZ time series $X_{\text{rGZ}}\left(t\right)$, its increment time series $\Delta X_{\text{rGZ}}\left(t\right)$ is defined as

$$\Delta X_{\text{rGZ}}\left(t\right) \equiv X_{\text{rGZ}}\left(t\right) - X_{\text{rGZ}}\left(t-1\right). \tag{A.0.1}$$

By definition, a value of $X_{\text{rGZ}}(t)$ at time t can be reconstructed by summing up (integrating) a sequence of $\Delta\, X_{\text{rGZ}}\left(i\right)$ from its initial value $X_{\text{rGZ}}\left(0\right)$ as

$$X_{\text{rGZ}}\left(t\right) = X_{\text{rGZ}}\left(0\right) + \sum_{i=1}^{t} \Delta X_{\text{rGZ}}\left(i\right). \tag{A.0.2}$$

Second, the decomposition of $X_{\text{rGZ}}\left(t\right)$ with its DRT components $X_{\text{DRT}}\left(t\right)$ and raw-MS components $X_{\text{rMS}}\left(t\right)$ is considered. Later, the simplified MS time series $X_{\text{MS}}\left(t\right)$ by eliminating overshoot components as well as a ballistic transient component of each MS from the raw-MS time series $X_{\text{rMS}}\left(t\right)$ is defined (Ozawa and Nomura, 2019) and analyzed for making relationships between DRT and MS clear, because detailed temporal structure of each MS waveform is out of interest here. Note that an overshoot is a small overrun component that is followed by a small return in the opposite direction to the MS immediately after the MS, after which the gaze position settles at the beginning of subsequent DRT motion. Let T_{rGZ} be the whole time interval (an inter-blink interval), on which $X_{\text{rGZ}}\left(t\right)$ is defined for $t \cdot \delta_s \subset T_{\text{rGZ}}$. Similarly, let T_{DRT} and T_{rMS} be the sets of time interval, for which we define

$$\Delta X_{\text{DRT}}\left(t\right) \equiv \begin{cases} \Delta X_{\text{rGZ}}\left(t\right) & \left(t \cdot \delta_s \subset T_{\text{DRT}}\right) \\ 0 & \left(t \cdot \delta_s \subset T_{\text{rMS}}\right) \end{cases} \tag{A.0.3}$$

$$\Delta X_{\text{rMS}}(t) \equiv \begin{cases} 0 & (t \cdot \delta_s \subset T_{\text{DRT}}) \\ \Delta X_{\text{rGZ}}(t) & (t \cdot \delta_s \subset T_{\text{rMS}}) \end{cases} \tag{A.0.4}$$

Note that

$$T_{\text{rGZ}} = T_{\text{DRT}} \cup T_{\text{rMS}} \tag{A.0.5}$$

$$T_{\text{DRT}} \cap T_{\text{rMS}} = \varnothing \tag{A.0.6}$$

As in Eq. (A.0.2), for given initial values of $X_{\text{DRT}}(t)$ and $X_{\text{rMS}}(t)$, $X_{\text{DRT}}(t)$ and $X_{\text{rMS}}(t)$ can be reconstructed from $\Delta X_{\text{DRT}}(t)$ and $\Delta X_{\text{rMS}}(t)$, respectively. That is, assuming these initial values are equal to the initial value $X_{\text{GZ}}(0)$ as

$$X_{\text{DRT}}(0) = X_{\text{rMS}}(0) = X_{\text{rGZ}}(0), \tag{A.0.7}$$

we have

$$X_{\text{DRT}}(t) = X_{\text{DRT}}(0) + \sum_{i=1}^{t} \Delta X_{\text{DRT}}(i)\,. \tag{A.0.8}$$

$$X_{\text{rMS}}(t) = X_{\text{rMS}}(0) + \sum_{i=1}^{t} \Delta X_{\text{rMS}}(i)\,. \tag{A.0.9}$$

Moreover, by taking the sum of Eqs. (A.0.3) and (A.0.4), we have

$$\Delta X_{\text{DRT}}(t) + \Delta X_{\text{rMS}}(t) \equiv \begin{cases} \Delta X_{\text{rGZ}}(t) & (t \cdot \delta_s \subset T_{\text{DRT}}) \\ \Delta X_{\text{rGZ}}(t) & (t \cdot \delta_s \subset T_{\text{rMS}}) \end{cases} \tag{A.0.10}$$

Thus, from Eq. (A.0.5), we have

$$\Delta X_{\text{DRT}}(t) + \Delta X_{\text{rMS}}(t) = \Delta X_{\text{rGZ}}(t) \tag{A.0.11}$$

for any $t \cdot \delta_s \subset T_{\text{rGZ}}$. By taking the sum of Eqs. (A.0.8) and (A.0.9), we also have

$$X_{\text{DRT}}(t) + X_{\text{rMS}}(t) = X_{\text{rGZ}}(t) + X_{\text{rGZ}}(0) \tag{A.0.12}$$

or

$$X_{\text{rGZ}}(t) = X_{\text{DRT}}(t) + X_{\text{rMS}}(t) - X_{\text{rGZ}}(0) \tag{A.0.13}$$

for any $t \cdot \delta_s \subset T_{\text{rGZ}}$. Eq. (A.0.13) indicates that we can reconstruct the corresponding time series $X_{\text{rGZ}}(t)$ from the decomposed components $X_{\text{DRT}}(t)$ and $X_{\text{rMS}}(t)$ with an initial value $X_{\text{rGZ}}(0)$.

Appendix B

Main Sequence

A linear relationship between the maximum amplitude and peak velocity of microsaccades (MS) is called a main sequence, which is often used to verify the correctness of the MS detection. To obtain plausible peak velocity, smoothed velocity defined as weighted moving average over five points is typically used in the E&K method (Engbert, 2006). For a given two-dimensional gaze position vector $\vec{x}(t) = (x(t), y(t))$, the smoothed velocity is defined as

$$\vec{v}(t) = \frac{\vec{x}(t + 2\,\Delta t) + \vec{x}(t + \Delta t) - \vec{x}(t - \Delta t) - \vec{x}(t - 2\,\Delta t)}{6\,\Delta t},$$

where Δt is a sampling interval. The peak velocity v_p was obtained as the maximum L^2-norm of the velocity vector during MS

$$v_p = \max\left(||\vec{v}(t)||\right) = \max\left(\sqrt{v_x^2(t) + v_y^2(t)}\right), (t_{on} \leq t \leq t_{off})$$

where v_x,v_y,t_{on},and t_{off} is a horizontal and vertical velocity of $\vec{v}$, and an onset or offset timing of any microsaccade, respectively. The maximus amplitude a_m was calculated as the maximum L^2-norm of the position vector during MS:

$$a_m = \max(||\vec{x}(t_{on}) - \vec{x}(t_i)||), (t_{on} < t_i <\leq t_{off})\,.$$

The main sequence calculated from the raw-MS time series data for all sample paths across all subjects obtained in this study was drawn using above equations in Fig. A1. Each blue dot in Fig. A1 represents a single MS event. The correlation coefficient between $\log a_m$ and $\log v_p$ was 0.93.

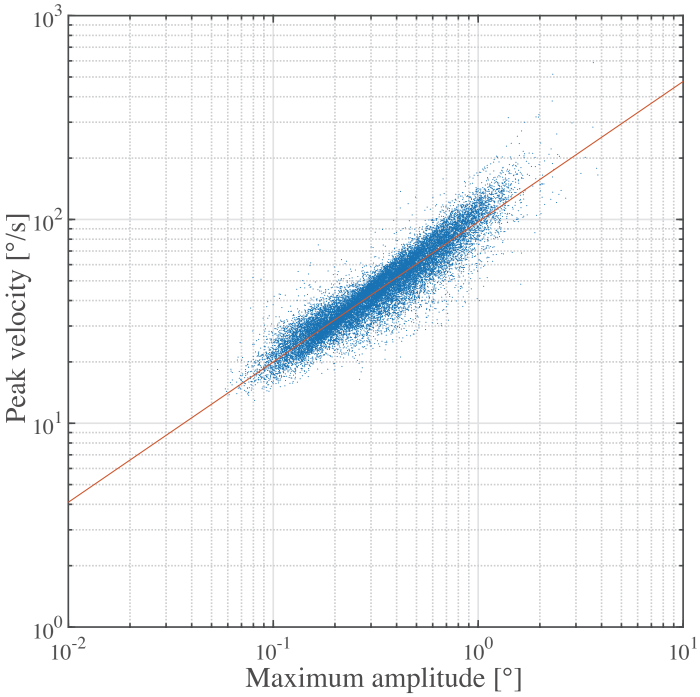

Figure A1: The main sequence of MS events detected from the raw MS time series data for all sample paths across all subjects. Blue dots are scattered pairs of maximum amplitude and peak velocity, and the orange line is the regression line.

Appendix C

Stochastic Process Representation for Fixational Eye Movements

In order to analyze gaze fluctuation with impulsive movements of microsaccades, it is necessary to construct a stochastic model that describes the impulse generation of the motor command. Moreover, after defining the impulse generator, solving the stochastic differential equation representing the intermittent control model is not always easy. Therefore, here, the following stochastic process that simplifies the solution of the intermittent control model is defined, and its dynamic characteristics are analyzed.

As a simplified intermittent control model,the approximate GZ time series G_t, which is a stochastic process consisting of an approximate DRT time series D_t and an approximate MS time series M_t, is considered. We assume that the increment of G_t is equal to the sum of the increments of D_t and M_t as following equation:

$$\Delta G_t = \Delta D_t + \Delta M_t. \tag{C.0.1}$$

In the rest of this section, after defining the approximate DRT time series D_t and the approximate MS time series M_t, the SDP of the increment as the mean square increment of D_t, the variance of M_t, and the SDP as the mean square increment of the approximate GZ time series G_t are calculated.

We define the approximate DRT time series D_t as a Wiener process with drift μ and infinitesimal variance σ^2:

$$D_t = \mu t + B_t, \tag{C.0.2}$$

where the expectation of the Wiener process B_t is zero. The increment of the Wiener process B_t in time interval τ can be defined as

$$\Delta_\tau B_t = B_{t+\tau} - B_t, \tag{C.0.3}$$

and its expectation and variance are

$$\begin{aligned} \mathrm{E}[\Delta_\tau B_t] &= 0, && \text{(C.0.4)} \\ \mathrm{Var}[\Delta_\tau B_t] &= \sigma^2 \tau. && \text{(C.0.5)} \end{aligned}$$

Then, given the increment of D_t in time interval τ as

$$\Delta_\tau D = \mu\tau + \Delta_\tau B_t, \tag{C.0.6}$$

one can calculate the expectation and variance of $Delta_\tau D$:

$$\begin{aligned} \mathrm{E}[\Delta_\tau D_t] &= \mu\tau, && \text{(C.0.7)} \\ \mathrm{Var}[\Delta_\tau D_t] &= \sigma^2 \tau. && \text{(C.0.8)} \end{aligned}$$

Therefore, the mean square increment of D_t, defined by the expectation of the squared increment $\Delta_\tau D_t$, is calculated as

$$\begin{aligned} \mathrm{E}[(\Delta_\tau D_t)^2] &= \mathrm{E}[\Delta_\tau D_t]^2 + \mathrm{Var}[\Delta_\tau D_t] && \text{(C.0.9)} \\ &= \mu^2\tau^2 + \sigma^2\tau. && \text{(C.0.10)} \end{aligned}$$

We suppose that an approximate MS time series model is consists of 2 types of Poisson processes M_t^+ which have positive constant amplitude w_+ and M_t^- which have negative constant amplitude w_-. In this way, the probability of the increments of each rightward/leftward MS process being equal to n_+w_+, n_-w_- is given by the probability of the number of rightward/leftward MS occurrences being equal to n_+, n_-, i.e.,

$$\begin{aligned} \mathrm{Prob}\left(\Delta_\tau M_t^+ = n_+ w_+\right) &= \frac{(\lambda\tau)^{n_+}}{n_+!} e^{-\lambda_+ \tau} \\ \mathrm{Prob}\left(\Delta_\tau M_t^- = n_- w_-\right) &= \frac{(\lambda\tau)^{n_-}}{n_-!} e^{-\lambda_- \tau} \end{aligned} \tag{C.0.11}$$

where the increment of each unidirectional MS process in time interval τ is defined as

$$\begin{aligned} \Delta_\tau M_t^+ &= M_{t+\tau}^+ - M_t^+, \\ \Delta_\tau M_t^- &= M_{t+\tau}^- - M_t^-. \end{aligned} \tag{C.0.12}$$

The expected value is obtained analytically as follows:

$$\begin{aligned} \mathrm{E}[\Delta_\tau M_t^+] &= \sum_{n_+=1}^{\infty} n_+ w_+ \frac{(\lambda\tau)^{n_+}}{n_+!} e^{-\lambda\tau} \\ &= w_+ \lambda_+ \tau, \end{aligned} \tag{C.0.13}$$

$$\begin{aligned} \mathrm{E}[\Delta_\tau M_t^-] &= \sum_{n_-=1}^{\infty} n_- w_- \frac{(\lambda\tau)^{n_-}}{n_-!} e^{-\lambda\tau} \\ &= w_- \lambda_- \tau. \end{aligned} \tag{C.0.14}$$

Here, defining the net increment of the MS process in time interval τ as

$$\Delta_\tau M_t = \Delta_\tau M_t^+ + \Delta_\tau M_t^-, \tag{C.0.15}$$

its expected value can be derived by Eq. (C.0.13), (C.0.14):

$$\mathrm{E}[\Delta_\tau M_t] = \mathrm{E}[\Delta_\tau M_t^+] + \mathrm{E}[\Delta_\tau M_t^-] \tag{C.0.16}$$

$$= (w_+\lambda_+ + w_-\lambda_-)\,\tau. \tag{C.0.17}$$

Similarly, since the expectation of the squared increment of the left/rightward MS process in time interval τ can be obtained analytically as

$$\begin{aligned} \mathrm{E}[\left(\Delta_\tau M_t^+\right)^2] &= \sum_{n=1}^{\infty} (n_+ w_+)^2 \frac{(\lambda\tau)^{n_+}}{n_+!} e^{-\lambda_+\tau} \\ &= w_+^2 \lambda_+^2 \tau^2 + w_+^2 \lambda_+ \tau, \end{aligned} \tag{C.0.18}$$

$$\begin{aligned} \mathrm{E}[\left(\Delta_\tau M_t^-\right)^2] &= \sum_{n=1}^{\infty} (n_- w_-)^2 \frac{(\lambda\tau)^{n_-}}{n_-!} e^{-\lambda_-\tau} \\ &= w_-^2 \lambda_-^2 \tau^2 + w_-^2 \lambda_- \tau, \end{aligned} \tag{C.0.19}$$

in addition to Eq. (C.0.13) and (C.0.14), these equations lead to the variance of the MS processes $\Delta_\tau M_t^+$ and $\Delta_\tau M_t^-$ in time interval τ:

$$\begin{aligned} \mathrm{Var}[\Delta_\tau M_t^+] &= \mathrm{E}[(\Delta_\tau M_t^+)^2] - \mathrm{E}[\Delta_\tau M_t^+]^2 \\ &= w_+^2 \lambda_+ \tau, \end{aligned} \tag{C.0.20}$$

$$\begin{aligned} \mathrm{Var}[\Delta_\tau M_t^-] &= \mathrm{E}[(\Delta_\tau M_t^-)^2] - \mathrm{E}[\Delta_\tau M_t^-]^2 \\ &= w_-^2 \lambda_- \tau. \end{aligned} \tag{C.0.21}$$

Since $\Delta_\tau M_t^+$ and $\Delta_\tau M_t^-$ are independent, the following equation for the variance of $\Delta_\tau M_t$ holds:

$$\begin{aligned} \mathrm{Var}[\Delta_\tau M_t] &= \mathrm{Var}[\Delta_\tau M_t^+] + \mathrm{Var}[\Delta_\tau M_t^-] \\ &= \left(w_+^2 \lambda_+ + w_-^2 \lambda_-\right) \tau. \end{aligned} \tag{C.0.22}$$

In order to focus on the net effect of MS, defining the net mean amplitude of MS $w\lambda$ and the coefficient $w^2\lambda$ of the variance of the net MS increment as

$$\begin{aligned} w\lambda &\equiv w_+\lambda_+ + w_-\lambda-, && \text{(C.0.23)} \\ w^2\lambda &\equiv w_+^2\lambda_+ + w_-^2\lambda_-, && \text{(C.0.24)} \end{aligned}$$

we can rewrite Eq. (C.0.16) and (C.0.22) as follows:

$$\begin{aligned} \mathrm{E}[\Delta_\tau M_t] &= w\lambda\tau, && \text{(C.0.25)} \\ \mathrm{Var}[\Delta_\tau M_t] &= w^2\lambda\tau, && \text{(C.0.26)} \end{aligned}$$

where,

$$\begin{aligned} w &= \frac{w_+^2\lambda_+ + w_-^2\lambda_-}{w_+\lambda_+ + w_-\lambda_-}, && \text{(C.0.27)} \\ \lambda &= \frac{(w_+\lambda_+ + w_-\lambda_-)^2}{w_+^2\lambda_+ + w_-^2\lambda_-}. && \text{(C.0.28)} \end{aligned}$$

Therefore, given the increment of the approximate GZ time series G_t in time interval τ,

$$\Delta_\tau G_t = \mu\tau + \Delta_\tau B_t + \Delta_\tau M_t, \tag{C.0.29}$$

since its expectation and variance holds:

$$\begin{aligned} \mathrm{E}[\Delta_\tau G_t] &= (\mu + w\lambda)\,\tau, && \text{(C.0.30)} \\ \mathrm{Var}[\Delta_\tau G_t] &= \left(\sigma^2 + w^2\lambda\right)\tau, && \text{(C.0.31)} \end{aligned}$$

we can derive the mean equare increment of G_t in time interval τ as

$$\begin{aligned} \mathrm{E}[(\Delta_\tau G_t)^2] &= \mathrm{E}[\Delta_\tau G_t]^2 + \mathrm{Var}[\Delta_\tau G_t] \\ &= (\mu + w\lambda)^2\,\tau^2 + \left(\sigma^2 + w^2\lambda\right)\tau \end{aligned} \tag{C.0.32}$$

We assume the following equation as a stable condition for normal fixation so that the mean error $\mathrm{E}[\Delta_\tau G_t]$ is sufficiently small:

$$\mathrm{E}[\Delta_\tau G_t] = \epsilon \;\; (|\epsilon| << 1)\,. \tag{C.0.33}$$

From Eq. (C.0.30), the following equation must be satisfied for the stable condition for any time scale τ:

$$\mu \approx -w\lambda, \tag{C.0.34}$$

In other words, the slope of the linear trend of DRT μ and the net mean amplitude of MS $w\lambda$ need to be balanced.

Using Eq. (C.0.10) and (C.0.32), we can derive the difference between the SDP of GZ process and the SDP of DRT process :

$$\begin{aligned}
\log \frac{\mathrm{E}[(\Delta_\tau G_t)^2]}{\mathrm{E}[(\Delta_\tau D_t)^2]} &= \log \frac{(\mu + w\lambda)^2 \tau + \sigma^2 + w^2\lambda}{\mu^2\tau + \sigma^2} && \text{(C.0.35)} \\
&\sim \log \left\{ 1 + \left(\frac{w}{\sigma} \right)^2 \lambda \right\}, && \text{(C.0.36)}
\end{aligned}$$

where, for the sake of approximation, it is assumed that μ is sufficiently small in the stable condition given as Eq. (C.0.34). Thus, if the linear trend of the DRT μ is sufficiently small and normal fixation is performed on a short time scale, we can find the difference between SDP of the GZ time series and SDP of the DRT time series, which is independent of time lag τ. Accordingly, applying the same analysis to the GZ time series and the DRT time series obtained by corresponding measurement of FEyeM, if real DRT have small linear trend $\hat{\mu}$, we expect similar reults to be obtained.

References

Abel, L.A., Parker, L., Daroff, R.B. and Dell'Osso, L.F. (1978). End-point nystagmus. Investigative ophthalmology & visual science, 17, 539-544.

Arnstein, D., Junker, M., Smilgin, A., Dicke, P.W. and Thier, P. (2015). Microsaccade control signals in the cerebellum. Journal of Neuroscience, 35, 8, 3403-3411. doi: 10.1523/JNEUROSCI.2458-14.2015

Becker, W. and Klein, H.M. (1973). Accuracy of saccadic eye movements and maintenance of eccentric eye positions in the dark. Vision research, 13, 1021-1034. doi: 10.1016/0042-6989(73)90141-7

Bertolini, G., Tarnutzer, A.A., Olasagasti, I., Khojasteh, E., Weber, K.P., Bockisch, C.J., Straumann, D. and Marti, S. (2013). Gaze holding in healthy subjects. PLoS One. 8, e61389. doi: 10.1371/journal.pone.0061389

Bögli, S. Y., Straumann, D., Schuknecht, B., Bertolini, G., and Tarnutzer, A. A. (2021). Cerebellar rebound nystagmus explained as gaze-evoked nystagmus relative to an eccentric set point: implications for the clinical examination. The Cerebellum, 20, 5, 751-759. doi: 10.1007/s12311-020-01118-6

Buonocore, A., Tian, X., Khademi, F. and Hafed, Z.M. (2021). Instantaneous movement-unrelated midbrain activity modifies ongoing eye movements. Elife, 10, p.e64150. doi: 10.7554/eLife.64150.sa2

Büttner, U. and Grundei, T. (1995). Gaze-evoked nystagmus and smooth pursuit deficits: their relationship studied in 52 patients. Journal of neurology, 242, 384-389. doi: 10.1007/BF00868394

Bridgeman, B. and Palca, J. (1980). The role of microsaccades in high acuity observational tasks. Vision research, 20, 813-817. doi: 10.1016/0042-6989(80)90013-9

Caffier, P. P., Erdmann, U., and Ullsperger, P. (2003). Experimental evaluation of eye-blink parameters as a drowsiness measure. European journal of applied physiology. 89, 319-325. doi: 10.1007/s00421-003-0807-5

Cannon, S.C. and Robinson, D. (1987). Loss of the neural integrator of the oculomotor system from brain stem lesions in monkey. Journal of neurophysiology. 57, 1383-1409. doi: 10.1152/jn.1987.57.5.1383

Collewijn, H., Erkelens, C.J. and Steinman, R.M. (1997). Trajectories of the human binocular fixation point during conjugate and non-conjugate gaze-shifts. Vision research, 37, 1049-1069. doi: 10.1016/S0042-6989(96)00245-3

Collins, J.J. and De Luca, C.J. (1993). Open-loop and closed-loop control of posture: a random-walk analysis of center-of-pressure trajectories. Experimental brain research, 95, 308-318. doi: 10.1007/BF00229788

Cornsweet, T. N. (1956). Determination of the stimuli for involuntary drifts and saccadic eye movements. JOSA. 46, 987-993. doi: 10.1364/JOSA.46.000987

Cunitz, R.J. and Steinman, R.M. (1969). Comparison of saccadic eye movements during fixation and reading. Vision research, 9, 683-693. doi: 10.1016/0042-6989(69)90125-4

Ditchburn, R.W. and Ginsborg, B.L. (1953). Involuntary eye movements during fixation. The Journal of physiology, 119, 1-17. doi: 10.1113/jphysiol.1953.sp004824

Eizenman, M., Cheng, P., Sharpe, J.A. and Frecker, R.C. (1990). End-point nystagmus and ocular drift: an experimental and theoretical study. Vision research. 30, 863-877. doi: 10.1016/0042-6989(90)90055-P

Engbert, R., and Kliegl, R. (2004). Microsaccades keep the eyes' balance during fixation. Phychological science. 15, 431-431. doi: 10.1111/j.0956-7976.2004.00697.x

Engbert, R. (2006). Microsaccades: A microcosm for research on oculomotor control, attention, and visual perception. Progress in brain research. 154, 177-192. doi: 10.1016/S0079-6123(06)54009-9

Engbert, R. and Mergenthaler, K. (2006). Microsaccades are triggered by low retinal image slip. Proceedings of the National Academy of Sciences, 103, 7192-7197. doi: 10.1073/pnas.0509557103

Ezenman, M., Hallett, P.E. and Frecker, R.C. (1985). Power spectra for ocular drift and tremor. Vision research, 25, 1635-1640. doi: 10.1016/0042-6989(85)90134-8

Findlay, J.M. (1971). Frequency analysis of human involuntary eye movement. Kybernetik, 8, 207-214. doi: 10.1007/BF00288749 Kheradmand A and Zee DS (2011) Cerebellum and ocular motor control. Frontiers in Neurology 2:53. doi: 10.3389/fneur.2011.00053

Hafed, Z.M., Goffart, L. and Krauzlis, R.J. (2009). A neural mechanism for microsaccade generation in the primate superior colliculus. science, 323(5916), pp.940-943. doi: 10.1126/science.1166112

Hafed, Z.M. (2011). Mechanisms for generating and compensating for the smallest possible saccades. European Journal of Neuroscience, 33(11), pp.2101-2113. doi: 10.1111/j.1460-9568.2011.07694.x

Hafed, Z.M., Yoshida, M., Tian, X., Buonocore, A. and Malevich, T. (2021). Dissociable cortical and subcortical mechanisms for mediating the influences of visual cues on microsaccadic eye movements. Frontiers in Neural Circuits, 15. doi: 10.3389/fncir.2021.638429

Heitmann, S., Breakspear, M., and Ferns, N. (2012). Muscle co-contraction modulates damping and joint stability in a three-link biomechanical limb. Frontiers in Neurorobotics, 5, 5. doi: 10.3389/fnbot.2011.00005

Ko, H.K., Poletti, M. and Rucci, M. (2010). Microsaccades precisely relocate gaze in a high visual acuity task. Nature neuroscience, 13, 1549-1553. doi: doi.org/10.1038/nn.2663

Leigh, R.J. and Zee, D.S. (2015). The neurology of eye movements, fifth edition. New York: Oxford University Press. doi: 10.1093/med/9780199969289.001.0001

Martinez-Conde, S., Macknik, S.L. and Hubel, D.H. (2004). The role of fixational eye movements in visual perception. Nature reviews neuroscience, 5, 229-240. doi: 10.1038/nrn1348

Martinez-Conde, S., Macknik, S.L., Troncoso, X.G. and Hubel, D.H. (2009). Microsaccades: a neurophysiological analysis. Trends in neurosciences, 32, 463-475. doi: 10.1016/j.tins.2009.05.006

Nakamagoe, K., Iwamoto, Y., and Yoshida, K. (2000). Evidence for brainstem structures participating in oculomotor integration. Science, 288, 5467, 857-859. doi: 10.1126/science.288.5467.857

Nyström, M., Hansen, D.W., Andersson, R. and Hooge, I. (2016). Why have microsaccades become larger? Investigating eye deformations and detection algorithms. Vision research. 118, 17-24. doi: 10.1016/j.visres.2014.11.007

Ono, H., and Barbeito, R. (1982). The cyclopean eye vs. the sighting-dominant eye as the center of visual direction. Perception & Psychophysics. 32, 201-210. doi: 10.3758/BF03206224

Otero-Millan, J., Castro, J.L.A., Macknik, S.L. and Martinez-Conde, S. (2014). Unsupervised clustering method to detect microsaccades. Journal of vision, 14, 18, 1-17. doi: 10.1167/14.2.18

Otero-Millan, J., Troncoso, X.G., Macknik, S.L., Serrano-Pedraza, I. and Martinez-Conde, S. (2008). Saccades and microsaccades during visual fixation, exploration, and search: foundations for a common saccadic generator. Journal of vision, 8, 21-21. doi: 10.1167/8.14.21

Otero-Millan, J., Macknik, S.L., Serra, A., Leigh, R.J. and Martinez-Conde, S. (2011). Triggering mechanisms in microsaccade and saccade generation: a novel proposal. Annals of the New York Academy of Sciences, 1233, 107-116. doi: 10.1111/j.1749-6632.2011.06177.x

Ozawa, M., and Nomura, T. (2019). Relationship between saccadic intrusions and a bimodal aspect of inter-microsaccadic intervals. In 2019 IEEE 1st Global Conference on Life Sciences and Technologies (LifeTech). 300-301. doi: 10.1109/LifeTech.2019.8883966

Ozawa, M., Suzuki, Y. and Nomura, T. (2022). Stochastic physiological gaze-evoked nystagmus with slow centripetal drift during fixational eye movements at small gaze eccentricities. Frontiers in Human Neuroscience. 16. doi: 10.3389/fnhum.2022.842883

Peel, T.R., Hafed, Z.M., Dash, S., Lomber, S.G. and Corneil, B.D. (2016). A causal role for the cortical frontal eye fields in microsaccade deployment. PLoS biology, 14(8), p.e1002531. doi: 10.1371/journal.pbio.1002531

Quinet, J., Schultz, K., May, P.J. and Gamlin, P.D. (2020). Neural control of rapid binocular eye movements: Saccade-vergence burst neurons. Proceedings of the National Academy of Sciences, 117, 29123-29132. doi: 10.1073/pnas.2015318117

Reschke, M.F., Somers, J.T., Feiveson, A.H., Leigh, R.J., Wood, S.J., Paloski, W.H. and Kornilova, L. (2006). Studies of the ability to hold the eye in eccentric gaze: measurements in normal subjects with the head erect. NASA Technical Reports Server. Available at: https://ntrs.nasa.gov/citations/20080026117 (Accessed December 20, 2021)

Robinson, D.A., Zee, D.S., Hain, T.C., Holmes, A. and Rosenberg, L.F. (1984). Alexander's law: Its behavior and origin in the human vestibul - ocular reflex. Annals of Neurology: Official Journal of the American Neurological Association and the Child Neurology Society, 16, 714-722. doi.org/10.1002/ana.410160614

Romano, F., Tarnutzer, A.A., Straumann, D., Ramat, S. and Bertolini, G. (2017). Gaze-evoked nystagmus induced by alcohol intoxication. The Journal of physiology. 595, 2161-2173. doi: 10.1113/JP273204

Rucci, M. and Poletti, M. (2015). Control and functions of fixational eye movements. Annual review of vision science, 1, 499-518. doi: 10.1146/annurev-vision-082114-035742

Shallo-Hoffmann J, Schwarze H, Simonsz HJ, and M ü hlendyck H. (1990) A reexamination of end-point and rebound nystagmus in normals. Investigative Ophthalmology & Visual Science, 31(2), 388-392.

Tarnutzer, A.A., Weber, K.P., Schuknecht, B., Straumann, D., Marti, S. and Bertolini, G. (2015). Gaze holding deficits discriminate early from late onset cerebellar degeneration. Journal of neurology, 262, 1837-1849. doi: 10.1007/s00415-015-7773-9

Versino, M., Hurko, O. and Zee, D.S. (1996). Disorders of binocular control of eye movements in patients with cerebellar dysfunction. Brain, 119, pp.1933-1950. doi: 10.1093/brain/119.6.1933

Whyte, C.A., Petrock, A.M. and Rosenberg, M. (2010). Occurrence of physiologic gaze-evoked nystagmus at small angles of gaze. Investigative ophthalmology & visual science. 51, 2476-2478. doi: 10.1167/iovs.08-3241

Willeke, K.F., Tian, X., Buonocore, A., Bellet, J., Ramirez-Cardenas, A. and Hafed, Z.M. (2019). Memory-guided microsaccades. Nature communications, 10, 1-14. doi: 10.1038/s41467-019-11711-x

Winterson, B.J. and Collewun, H. (1976). Microsaccades during finely guided visuomotor tasks. Vision research, 16, 1387-1390. doi: 10.1016/0042-6989(76)90156-5

Publication

Journal Paper

International Journal Paper

Makoto Ozawa, Yasuyuki Suzuki, and Taishin Nomura. Stochastic physiological gaze-evoked nystagmus with slow centripetal drift during fixational eye movements at small gaze eccentricities. *Frontiers in Human Neuroscience.* 16, 2022. doi: 10.3389/fnhum.2022.842883

Journal Papers (for reference only)

International Journal Papers

Haruhiko Adachi, Makoto Ozawa, Satoshi Yagi, Makoto Seita, and Shigeru Kondo. Pivot burrowing of scarab beetle (Trypoxylus dichotomus) larva. *Scientific Reports.* 11, 1, 1-6, 2021. doi: 10.1038/s41598-021-93915-0

Shinjiro Mita, Nayuta Sato, Morio Fujimoto, Shunichi Sugimoto, Taiga Fujimoto, Makoto Ozawa, Hiroki Fukunaga, Zenjiro Mita, and Satoru Iwasaki. 5 Lanes 5 Fingers Touch-typing Interface “ParoTone” for Efficient Sensorimotor Learning: Musical Performance Acquisition Much Faster than Piano. Accepted in *International Journal of Human-Computer Interaction.*

Domestic Journal Papers

宝財吉拉呼, 加賀谷文紀, 松井瑞季, 津野将行, 小澤誠, 野村泰伸, 塚田章, 前田義信. 視覚探索時の注視点ネットワークが示すスモールワールド性. 電子情報通信学会論文誌, J103-A, 7, 142-151, 2020.

小寺龍之介, 津野将行, 小澤誠, 野村泰伸, 塚田章, 前田義信. 視覚探索を最適化する注視点時系列モデルの提案. 生体医工学, 56, 5, 190-197, 2018. doi: 10.11239/jsmbe.56.190

Conference Papers

International Conferences

Makoto Ozawa, Yasuyuki Suzuki, and Taishin Nomura. Gaze-evoked nystagmus with centripetal drifts and centrifugal microsaccades during gaze fixation and its minimal neuromechanical model. *Neural Coding 2021 14th International Neural Coding Workshop*, 36, 2021.

Makoto Ozawa and Taishin Nomura. Relationship between saccadic intrusions and a bimodal aspect of inter-microsaccadic intervals. *2019 IEEE 1st Global Conference on Life Sciences and Technologies (LifeTech)*, 300-301, 2019. doi: 10.1109/LifeTech.2019.8883966

Domestic (Japanese) Conferences

小澤誠, 鈴木康之, 野村泰伸. ジャンプ拡散過程を用いた固視微動のニューロメカニカルモデル. 第30回日本神経回路学会全国大会. O2-04, 1-2, オンライン開催 (2020.12).

小澤誠, 野村泰伸. 固視微動の間欠制御モデル. 電子情報通信学会技術研究報告, MBE2019-93, 69, 電気通信大学 (開催中止, 技報発行あり)(2020.3).

小澤誠, 野村泰伸. ヒト固視中の視線ゆらぎの動特性解析. 計測自動制御学会 ライフエンジニアリング部門シンポジウム 2018, 2D2-5, 65, 会津大学 (2018.9).

Conference Papers (for reference only)

Domestic (Japanese) Conferences

前田義信, 小澤誠, 野村泰伸, 塚田章. 複雑ネットワークの観点から視覚探索が効率的であることを考察する. 電子情報通信学会技術研究報告, MBE2020-23, 18-23, オンライン開催 (2020.9).

加賀谷文紀, 松井瑞季, 中山周明, 津野将行, 宝財吉拉呼, 小澤誠, 野村泰伸, 塚田章, 前田義信. 視覚探索時の注視点ネットワーク分析の試み. 2019年度電子情報通信学会信越支部大会. 7D-1, 122, 長岡技術科学大学 (2019.9).

松井瑞季, 津野将行, 小澤誠, 野村泰伸, 塚田章, 前田義信. 視覚探索時に測定された注視点移動長の固視微動とサッカードへの分類. 電子情報通信学会技術研究報告. MBE2019-7, 33-38, 新潟大学 (2019.5).

前田義信, 小寺龍之介, 津野将行, 小澤誠, 野村泰伸, 塚田章. 視覚探索時の眼球運動のモデリングの試み, 電子情報通信学会技術研究報告, CAS2018-40, 19-24, 東北大学 (2018.10).

松井瑞季, 津野将行, 小寺龍之介, 小澤誠, 野村泰伸, 塚田章, 前田義信. 効率的な視覚探索を可能とする注視点移動長モデルの提案. 第38回日本生体医工学会甲信越支部大会. 6-7, 新潟大学五十嵐キャンパス (2018.10).

小寺龍之介, 小澤誠, 野村泰伸, 塚田章, 前田義信. 視覚探索時における眼球運動の頻度分布の検討. MBE2018-5, 23-26, 富山大学 (2018.5).

Conferences

Domestic (Japanese) Conferences

小澤誠, 野村泰伸. ドリフトとマイクロサッケードの協調的な相反関係. 生体医工学シンポジウム2017. 信州大学 (2017.9).

小澤誠, 野村泰伸. 固視微動におけるマイクロサッケードとドリフトの相反的振舞い: ヒト眼球姿勢保持の神経制御メカニズム. 第11回Motor Control研究会. 中京大学 (2017.8).

Conferences (for reference only)

Domestic (Japanese) Conferences

加賀谷文紀, 橋本帆波, 王禹萱, 小澤誠, 野村泰伸, 塚田章, 前田義信. Efficient Visual Search Explained by Small-World Feature of Gaze Position Network. 生体医工学シンポジウム. 1A-11, オンライン開催 (2021.9).

橋本帆波, 松井瑞季, 小澤誠, 野村泰伸, 塚田章, 前田義信. 視覚探索における探索時間に影響を与える要因の解析. 第60回日本生体医工学会大会. O3-5-1-4, オンライン開催 (2021.6).

松井瑞季, 中山周明, 加賀谷文紀, 小澤誠, 野村泰伸, 塚田章, 前田義信. 視覚探索における眼球運動および探索戦略の傾向. 生体医工学シンポジウム2020. 2A-05, オンライン開催 (2020.9).

中山周明, 松井瑞季, 加賀谷文紀, 小澤誠, 野村泰伸, 塚田章, 前田義信. 視覚探索時におけるマイクロサッケードの抑制に関して, 生体医工学シンポジウム2020. 2A-04, オンライン開催 (2020.9).

加賀谷文紀, 松井瑞季, 中山周明, 小澤誠, 野村泰伸, 塚田章, 前田義信. 視覚探索における注視点の軌跡が示すスモールワールド性の検証, 第59回日本生体医工学会大会. PO-2-052, 岡山コンベンションセンター中止でオンライン開催 (2020.5).

小寺龍之介, 津野将行, 小澤誠, 野村泰伸, 塚田章, 前田義信：視覚探索を最適化する注視点時系列モデルの提案. 生体医工学シンポジウム 2018. 1A-20, 名古屋工業大学 (2018.9).

Acknowledgment

I would like to sincerely appreciate my supervisor, Prof. Taishin Nomura, for supporting my Ph.D. course works. His breadth and depth of knowledge, vast experience and precise advice have helped me succeed in my research between engineering and neuroscience. Without his kind support, my Ph.D. course would not have been completed.

I would like to thank Prof. Osamu Oshiro and Prof. Ken Kiyono for serving on my dissertation committee. Their critical remarks helped me to improve my dissertation.

I would like to thank Associate Prof. Yasuyuki Suzuki for discussing and double-checking my model study. His kindness and mathematical skilIs were essential in building the model.

I thank Assistant Prof. Matija Milosevic and Specially Appointed Prof. Toru Nakamura for the discussion. Critical talking with them helped my better understanding and improvement.

I thank Drs. Yasushi Kobayashi and Ken-ichi Okada for their initial guidance for the experimental setup.

Daily life in the Ph.D. course with the other Ph.D. students, Dr. Akihiro Nakamura and Mr. Robert Martins de Freitas, and the other lab members was exciting and enjoyable. I thank them a lot.

Collaborative research of eye movements in visual search with Prof. Yoshinobu Maeda and students in Maeda Laboratory at Niigata University. let me broaden my perspective of human vision. I thank all of them.

The Humanware Innovation Program, an interdisciplinary degree program established by Osaka University, gave me opportunities to try extending beyond the disciplinary boundaries and learn the way of making an innovation. I thank the faculty members, other staff, and students in the program.

The first step in my academic life began as an undergraduate student in Ichino Laboratory at Kindai University. Under Dr. Takatoshi Ichino, with Dr. Satoshi Takatori, I studied nonlinear science and nonequilibrium physics, and for the first time I felt the joy of becominig a researcher and engineer. I thank both of them and the other faculty members at Kindai University.

I have to appreciate financial support: Humanware Innovation Program (Program for Leading Graduate Schools) and RA (Research Assistant) in Osaka University, the scholarship by Sumitomo Chemical CO., Ltd., and the Research Fellowship for Young Scientists by JSPS (Japan Society for the Promotion of Science). Without these financial supports, I would not have been able to concentrate on and complete my Ph.D. course.

Finally, I would like to say special thanks to my mother, Chihiro, who raised my older sister and me single-handedly, and my older sister, Nao, who financially supported me to get into the undergraduate university. My father, Minoru, a Haiku poet, encouraged me by sending his latest Haiku journals and books. I thank him. Spending time with my partner, Akari, gave me peace of mind. I greatly thank her.